



CLIC – Note – 1158

## COUPLED RF-THERMO-STRUCTURAL ANALYSIS OF CLIC TRAVELING WAVE ACCELERATING STRUCTURES

K. Papke<sup>1</sup>, C. Rossi<sup>1</sup> and G. Burt<sup>1,2</sup>

<sup>1</sup>CERN, Geneva, Switzerland

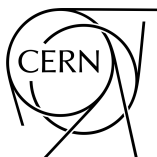
<sup>2</sup>Lancaster University, Lancaster, United Kingdom

### Abstract

Temperature changes in the CLIC accelerating structure lead to unwanted deformation. One of the aims of the CLIC module team is to optimize the necessary cooling system. The extended thermal program of the module was complemented by these thermal studies on real RF structures tested in X-band high-power test stands at CERN, Geneva (CH). The impact of thermal expansion on the RF characteristics of CLIC traveling wave accelerating structures is studied. The simulation setup in COMSOL is described in much detail. The necessary geometry simplifications are pointed out, mesh configurations are discussed by means of convergence studies, as well as important post-processing quantities are introduced which are common for characterizing traveling wave structures. The present report treats two different prototypes of the TD26\_R05 design, a damped traveling wave accelerating structure using 26 cells and two matching cells, with a bending radius of 0.5 mm being applied. One of these prototypes is currently being conditioned in the Xbox2 test stand.

Geneva, Switzerland  
16 September 2020





# Coupled RF-Thermo-Structural Analysis of CLIC Traveling Wave Accelerating Structures

Kai Papke, Carlo Rossi, Graeme Burt  
CERN, CH-1211 Geneva, Switzerland

Keywords: CLIC, Temperature control, Thermo-mechanical stability

---

---

## Summary

Temperature changes in the CLIC accelerating structure lead to unwanted deformation. One of the aims of the CLIC module team is to optimize the necessary cooling system. The extended thermal program of the module was complemented by these thermal studies on real RF structures tested in X-band high-power test stands at CERN, Geneva (CH). The impact of thermal expansion on the RF characteristics of CLIC traveling wave accelerating structures is studied. The simulation setup in COMSOL is described in much detail. The necessary geometry simplifications are pointed out, mesh configurations are discussed by means of convergence studies, as well as important post-processing quantities are introduced which are common for characterizing traveling wave structures. The present report treats two different prototypes of the TD26\_R05 design, a damped traveling wave accelerating structure using 26 cells and two matching cells, with a bending radius of 0.5 mm being applied. One of these prototypes is currently being conditioned in the Xbox2 test stand.

---

# Contents

<b>1</b>	<b>Introduction</b>	<b>3</b>
<b>2</b>	<b>Geometry</b>	<b>3</b>
2.1	Simplification . . . . .	3
2.2	Cooling Path . . . . .	5
2.3	Preparation . . . . .	5
<b>3</b>	<b>Physics</b>	<b>7</b>
3.1	Electromagnetic Waves . . . . .	7
3.2	Heat Transfer and Pipe Flow . . . . .	15
3.3	Structural Deformation . . . . .	25
3.4	Moving Mesh and Port Displacement . . . . .	29
<b>4</b>	<b>Studies on Perturbed Structures</b>	<b>30</b>
4.1	Variation of Flow Rate . . . . .	31
4.2	Cooling Circuits . . . . .	33
4.3	Linear Scaling . . . . .	34
4.4	Frequency Tuning by Water Temperature . . . . .	35
<b>5</b>	<b>Conclusions</b>	<b>36</b>
5.1	Simulation approach . . . . .	37
5.2	Pipe flow . . . . .	37
5.3	RF results . . . . .	37
<b>A</b>	<b>Parameters</b>	<b>40</b>
<b>B</b>	<b>Selections</b>	<b>42</b>

# 1 Introduction

The CLIC accelerating structures is fabricated with very tight manufacturing and positioning tolerances, both of which are sensitive to temperature changes. A careful design of the cooling system is thus mandatory to ensure stable operation and the desired performance of the machine, taking into account that these components provide the largest power density of the accelerator complex.

The impact of thermal expansion on the RF characteristics of CLIC traveling wave accelerating structures is studied. The simulation setup in COMSOL is described in much detail. The necessary geometry simplifications are pointed out, mesh configurations are discussed by means of convergence studies, as well as important figures of merit are introduced which are common for characterizing traveling wave structures. The present report deals with two different prototypes of the TD26\_R05 design, a damped traveling wave accelerating structure employing 26 cells and two matching cells, with a waveguide corner radius of 0.5 mm being applied. One of these prototypes is currently being conditioned in the Xbox2 test stand.

## 2 Geometry

Two different prototypes are subjected to coupled thermal, structural, and RF simulations both derived from the TD26\_R05 design, a damped CLIC traveling wave accelerating structure using 26 cells and two matching cells. The waveguides of each cell provides a bending radius of 0.5 mm towards the propagation direction. The first prototype denoted as TD26\_R05\_CC considers a single accelerating structure equipped with compact couplers [1]. The waveguides are shortened with respect to the original RF design which yield a phase advance per cell slightly lower than 120 deg. The second prototype denoted as TD26\_R05\_SS considers two combined accelerating structures equipped with compact couplers and manifolds comprising SiC absorbers. The generally referred super structure is currently being conditioned and tested in Xbox2.

### 2.1 Simplification

Figs. 1 and 2 show the original prototype assemblies together with the corresponding simplified model. All modifications of the original models have been carried out using SPACECLAIM [2] and can be summarized as follows:

- Components were suppressed which are expected to have a marginal impact on the studies, for instance, flanges, connectors, nuts, bellows, and washers.
- The tuning holes were filled.
- Cooling pipes and associated details were removed. Note, they are represented by separate line elements in the simulations.
- The alignment and orientation of various waveguides required corrections.



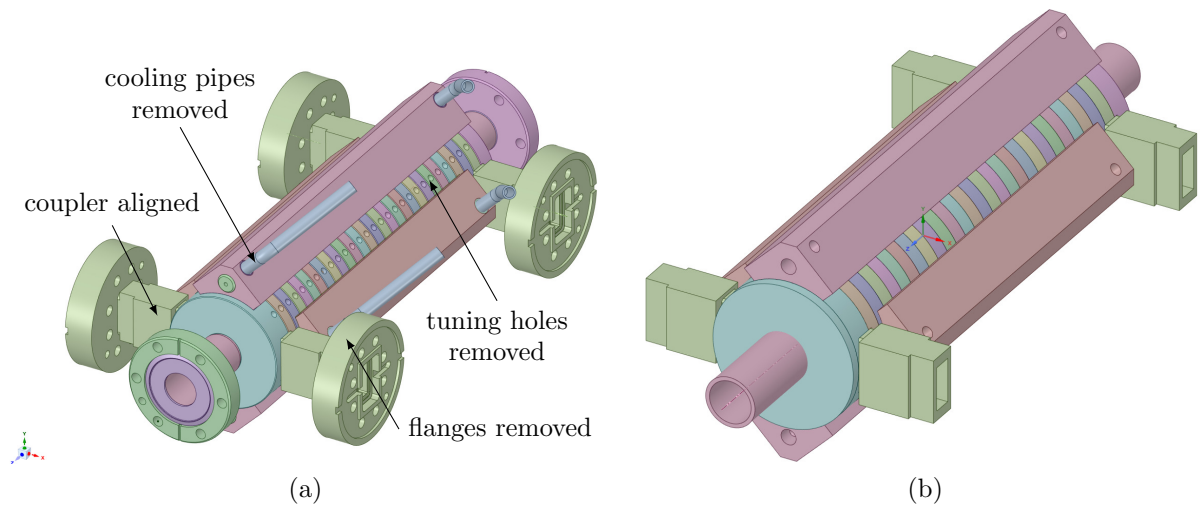


Figure 1: (a) Original geometry of the TD26\_R05\_CC prototype assembly, with the highlighted features being modified, removed or replaced for the studies. (b) Simplified model. Note, the holes reserved for cooling pipes are only kept for reasons of illustration.

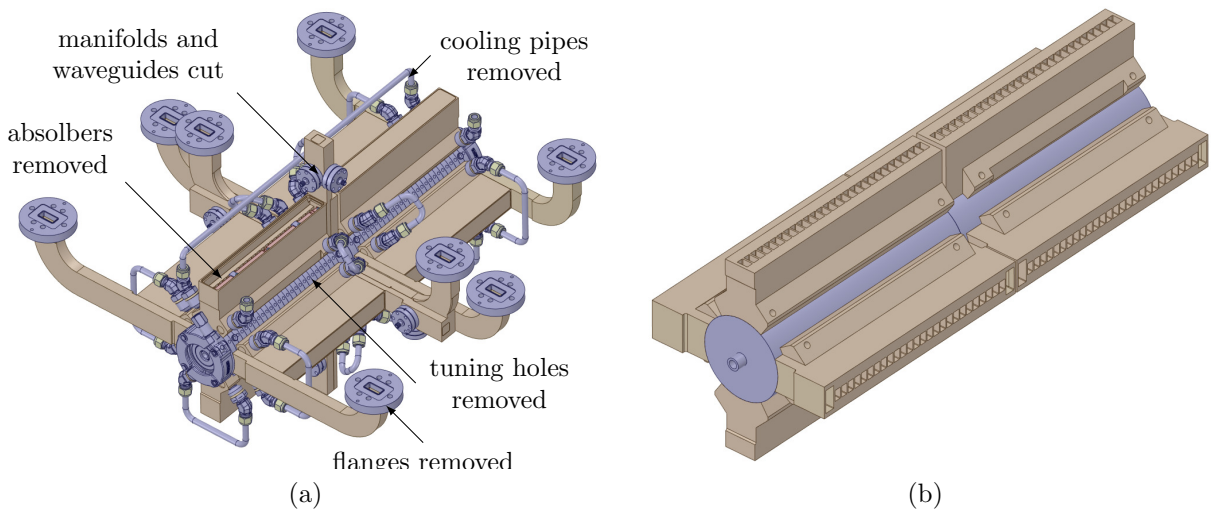


Figure 2: (a) Original geometry of the TD26\_R05\_SS prototype assembly, with the highlighted features being modified, removed, or replaced for the studies. (b) Simplified model. Note, the holes reserved for cooling pipes are only kept for reasons of illustration.

- Slider surface were removed. Note, disks of the TD26\_R05\_CC prototype assembly provide a very small chamfer on the inner surface for manufacturing reasons, only. For the studies of interest, such details can be ignored.
- Interfaces between different parts were much simplified. Hence, any holes, groves, bending or other small details in between the geometry parts were removed. This reduces significantly the complexity of resulting meshes.
- In order to achieve a smooth continuation of the waveguides provided by the cavity

disks, a bending radius of 0.5 mm is applied at the waveguide edges of the manifolds towards propagation direction.

- Manifolds and waveguides of the TD26\_R05\_SS prototype assembly are cut to a common length while removing the SiC absorbers. Note, the present studies focus on the fundamental mode, only. Mechanisms related to higher-order modes are excluded.
- All cavity disks of an accelerating structure were unified to a single geometry part.

It is important to note that the complementary part, that is the inner cavity volume filled with vacuum, is not created in SPACECLAIM but rather directly in the particular simulation tool, hence, in this case COMSOL. This avoids self-intersection errors which often occur when transferring complex geometries between different software despite the fact that a common geometry file standard, such as `*.sat` or `*.stp` is used. For this reason, the models are particularly modified in that the interfaces between different parts are as simple as possible while the number of interfaces is minimized.

## 2.2 Cooling Path

Coupled simulation of three-dimensional flow and heat transfer inside the cooling channels as well as the surrounding structure are computationally expensive. Often a semi-analytic approach is used to approximately determine the heat transfer coefficient between the coolant and solid. This approach is typically applied in ANSYS or CST. In contrast, COMSOL provides a fully consistent approach combining the one-dimensional pipe flow with three-dimensional heat transfer in the surrounding structure. Both approaches, which are further described in Sec. 3.2 allow to represent the cooling circuits by paths, hence, line elements as shown in Fig. 3. The positioning and properties of the cooling channels are important aspects for the structure design. This way, it becomes very convenient to optimize the cooling system and parameters. Figs. 3(a) and 3(b) show possible circuit configurations using one inlet and outlet for each prototype assembly.

Though both prototype assemblies are based on the same RF design, the number and location of holes preserved for the cooling channels differ as illustrated in Fig. 3(a) and (b) by corresponding cross-sections at the level of input couplers. Any cooling path can be defined based on the highlighted transverse coordinates together with longitudinal positions which are summarized in Tables 1 and 2 in Appendix A.

Due to their simplified representation by line elements, the holes preserved for the cooling channels are not required neither for the semi-analytic nor for the fully consistent approach. Consequently, these features are not present in considered geometries which has the advantage that a modification of the pipe diameter does not imply to modify the geometry. It is worth noting that a certain mesh refinement around the cooling channels is required for accurate heat flow calculations.

## 2.3 Preparation

Independent of the simplification steps described in Sec. 2.1, the geometry requires further preparation after importing in the particular simulation software. For instance, the volume

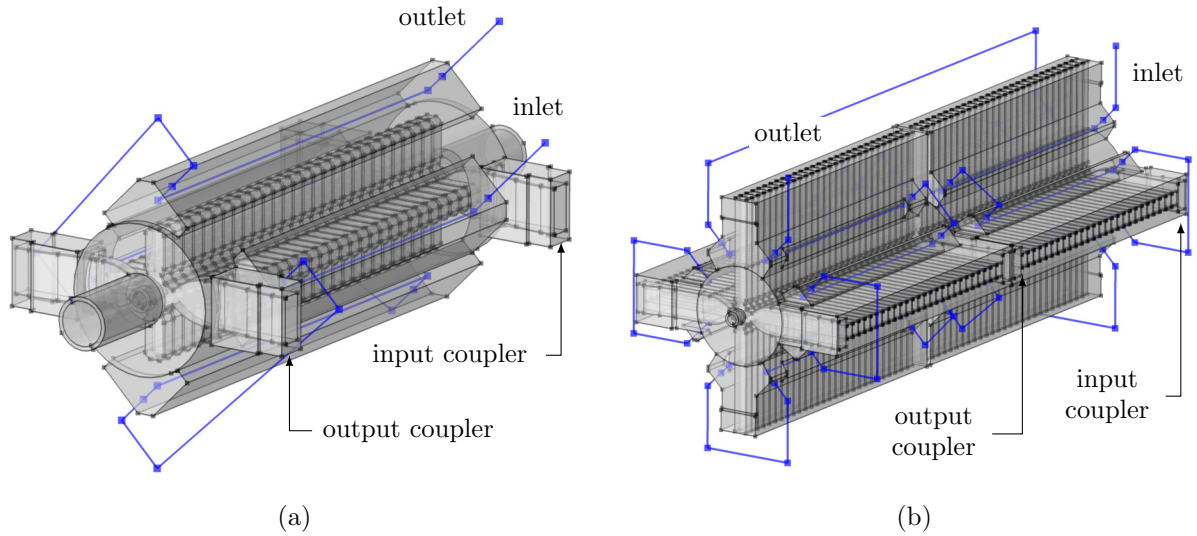


Figure 3: Cooling paths modeled by line elements. (a) TD26\_R05\_CC and (b) TD26\_R05\_SS prototype assembly.

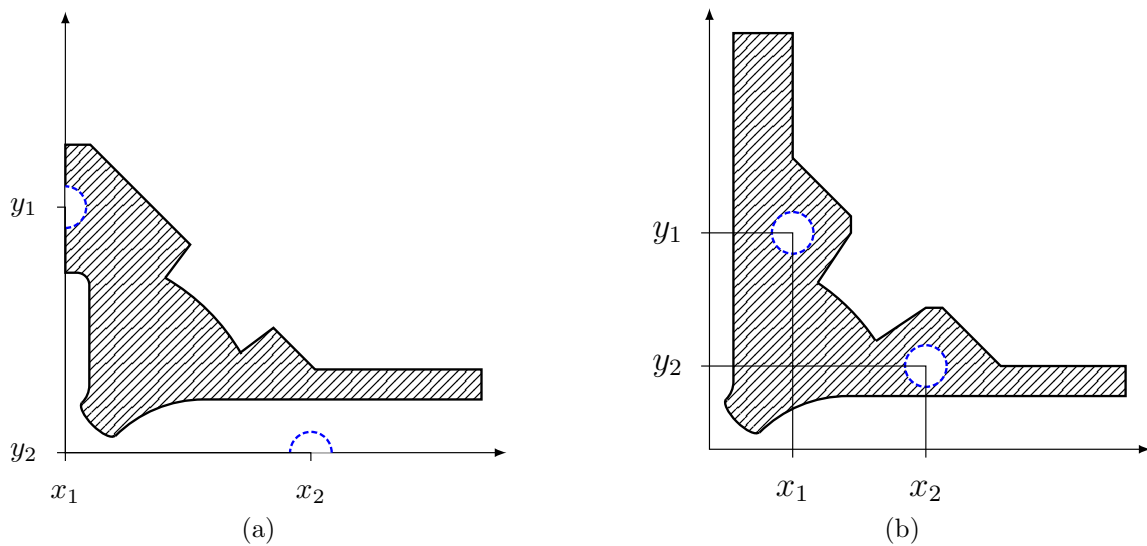


Figure 4: Cross-sectional view of the traveling wave structure at the input coupler which is located at the bottom right of the shown quadrant. The coordinate axes represent symmetry planes, with the transverse coordinates of the cooling pipes being highlighted. (a) TD26\_R05\_CC and (b) TD26\_R05\_SS prototype assembly.

surrounded by the structure and filled with vacuum is part of this preparation step in order to avoid self intersecting geometries and, thus, meshing errors. Fig. 5 sketches the workflow applied in COMSOL. Note, this process strongly depends on the features provided by the particular software.

After importing the simplified prototype assemblies from Sec. 2.1, the different parts, such as disks, cooling blocks, and couplers first become unified. A subsequent healing process

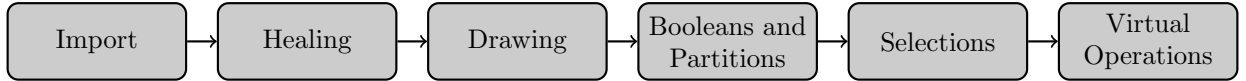


Figure 5: Geometry preparation in COMSOL.

removes slider surfaces and short edges from the structure before its complementary geometry is created. The latter one constitutes the vacuum part used for the RF simulation.

Additional geometry parts are added such as a line and cylinder along the particle beam. Likewise cylinders are placed at the preserved locations of the cooling channels while the circuit itself is defined by a polygon whose coordinates are stored in a separate file (`*CoolingCircuit.txt`). Other than the cooling path and vacuum part, all additional geometry parts serve for mesh refinements in order to provide a higher accuracy of the electromagnetic field quantities along the particle beam propagation as well as the heat transfer coefficient between the coolant and surrounding solid. Several Boolean operations and partitions are applied to resolve overlaps, define interfaces, associate domains of common material to objects which are eventually split into virtual domains for the meshing process. Generally, there are two strategies to finalize a CAD model. Either interfaces between different geometry parts are shared such that continuity of the field and fluxes is preserved or the coinciding boundaries are paired but still belong to the individual domain. The choice has consequences in the geometry description, physics settings, and mesh [3].

Predefined selections of multiple domains boundaries and edges facilitate the settings for physics, mesh, and post processing. They further ensure a consistent configuration even after modifying or replacing the model provided it is similar to the original one. A complete list of selections by means of the TD26\_R05\_CC prototype assembly is given in Tables 3–6 in Appendix A.

Finally, virtual operations are used to compose surfaces, ignore edges or dedicate specific geometry part for meshing, only, such as the cooling channels. They are generally used to improve the mesh quality by avoiding narrow vertices, short edges, thin surfaces or other small features [4]. In particular, surface compositions of the iris boundaries significantly improve the mesh quality.

## 3 Physics

### 3.1 Electromagnetic Waves

The CLIC traveling wave structures are fed via two symmetrically arranged waveguide couplers as illustrated in Fig. 6a. While propagating through the structure, a fraction of energy carried by the emerged wave is dissipating into the cavity wall due to the finite conductivity. The remaining fraction of energy is extracted by two waveguide couplers using the same arrangement as for the input side. Note, the unloaded case shall be considered in the present studies, that is, no energy transfer to the particle bunch is involved.

The wave propagation can be described by the wave equation for the electric field intensity

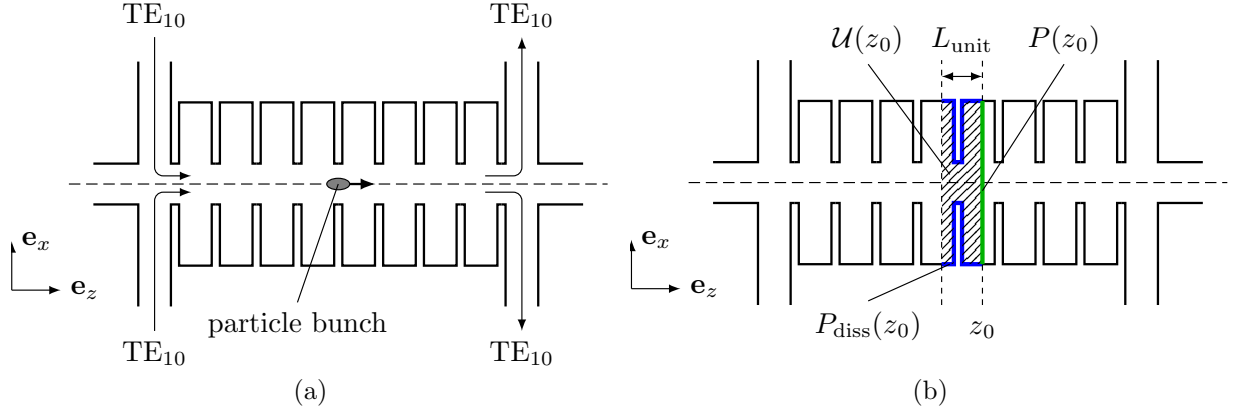


Figure 6: .

in frequency domain according to

$$\nabla \times \nabla \times \mathbf{E} - k_0^2 \mathbf{E} = 0, \quad \mathbf{r} \in \Omega_{\text{vac}}, \quad (1)$$

The spatial domain  $\Omega_{\text{vac}}$  refers to the inner volume of the cavity filled with vacuum (Appendix A, Table 6). Accordingly, the wave propagates at the speed of light which is described by the wave number  $k_0 = \omega/c_0$  where  $\omega = 2\pi f$  is the angular frequency. The latter one is given by the frequency of the exciting  $\text{TE}_{10}$  waveguide mode at both input ports which satisfy the following eigenvalue problem on the particular port boundary  $\partial\Omega_p$

$$\nabla \times \nabla \times H_n \mathbf{n} + (\beta^2 - k_0^2) H_n \mathbf{n} = 0, \quad \mathbf{r} \in \partial\Omega_p, \quad (2)$$

with  $H_n$  being the component of the magnetic field intensity perpendicular to the boundary and in parallel to the normal unit vector  $\mathbf{n}$ . The generalized index  $n$  specifies the periodicity of the solution in both transverse direction spanning the port boundary. Note, the frequency is chosen such that only the  $\text{TE}_{10}$  mode is able to propagate through the waveguide according to the propagation constant  $\beta$  perpendicular to the boundary  $\partial\Omega_p$ . The eigenmode solution of (2) at both input and output ports serve as boundary conditions for the problem (1). Though the output ports do not provide any inward propagating wave, the solutions are required to describe an infinite continuation of the corresponding waveguide. Fig. 7(a) shows the port notation by means of the TD26\_R05\_CC prototype assembly. Port 1 and 2 serve as input ports providing the  $\text{TE}_{10}$  mode, both at the same face while port 3 and 4 serve as the output for the traveling wave. It is important to note that problem 2 does provides a unique solution for the specific mode except for a phase which can be a multiple of  $\pi$ . It is, thus possible that an artificial phase offset of  $\pi$  may be required between the input ports in order to excite the traveling wave in the structure. This is typically verified by an initial RF simulation of only the port modes.

In order to account for energy dissipation in the cavity wall an impedance condition is applied at the common boundary between the vacuum filled domain  $\Omega_{\text{vac}}$  and surrounding structure  $\partial\Omega_{\text{solid}}$ , which is given by

$$\mathbf{n} \times \mathbf{E}(\mathbf{r}) = Z_s \mathbf{n} \times \mathbf{H}(\mathbf{r}) \quad \mathbf{r} \in \partial\Omega_{\text{solid}} \cap \partial\Omega_{\text{vac}}. \quad (3)$$

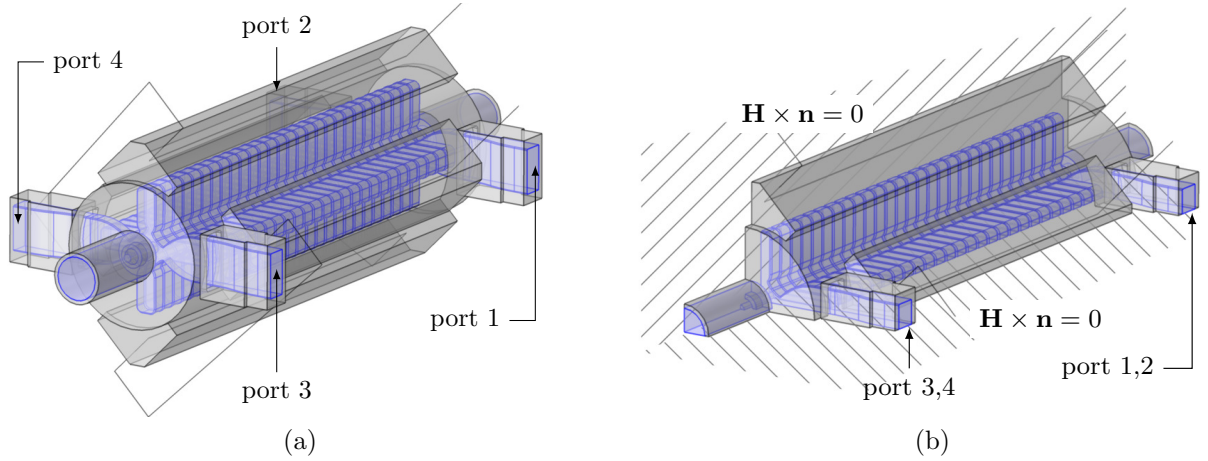


Figure 7: Boundary conditions for the problem (1). The incident  $TE_{10}$  mode provided via port 1 and 2 are at the same phase. The remaining fraction of energy carried by the emerged wave traveling through the structure which is not dissipating into the cavity wall is extracted by the passive ports 3 and 4. (a) Full model of the TD26\_R05\_CC prototype assembly. (b) Simplified model of (a) with perfect magnetic boundaries applied in both symmetry planes. A single input and output port are required to describe the original problem.

The surface impedance of normal conductors calculates as [5, p. 429]

$$Z_s = (1 + j) \sqrt{\frac{\mu_0 \omega}{2\sigma}} = \frac{1 + j}{\sigma \delta}, \quad (4)$$

with the permittivity constant  $\mu_0$ , angular frequency  $\omega$ , electric conductivity  $\sigma$  given by the material, and penetration depth  $\delta$ .

Symmetries of the model allow to significantly reduce the problem size. Typically the structures are designed by considering only a quarter as illustrated in Fig. 7(b). The tangential components of the magnetic field intensity  $\mathbf{H}$  provided by traveling wave must vanish at these symmetry planes  $\partial\Omega_{\text{sym}}$  according to

$$\mathbf{H}(\mathbf{r}) \times \mathbf{n} = 0, \quad \mathbf{r} \in \partial\Omega_{\text{sym}}, \quad (5)$$

with the unit vector  $\mathbf{n}$  being normal to the particular boundary. It is worthwhile to note that the symmetry planes get lost once the deformed structure is considered since the distribution of temperature and, thus, thermal expansion are generally not symmetric. For this reason, only the complete model shall be considered in the following.

Using the previous notation of active and passive ports, the scattering parameter to characterize the RF reflection and transmission are defined as

$$s_{11} = \frac{\iint_{p_1} (\mathbf{E} - \mathbf{E}_{p_1}) \cdot \mathbf{E}_{p_1}^* dA + \iint_{p_2} (\mathbf{E} - \mathbf{E}_{p_2}) \cdot \mathbf{E}_{p_2}^* dA}{\iint_{p_1} \mathbf{E}_{p_1} \cdot \mathbf{E}_{p_1}^* dA + \iint_{p_2} \mathbf{E}_{p_2} \cdot \mathbf{E}_{p_2}^* dA} \quad (6)$$

$$s_{21} = \frac{\iint_{p_3} \mathbf{E} \cdot \mathbf{E}_{p_3}^* dA + \iint_{p_4} \mathbf{E} \cdot \mathbf{E}_{p_4}^* dA}{\iint_{p_3} \mathbf{E}_{p_3} \cdot \mathbf{E}_{p_3}^* dA + \iint_{p_4} \mathbf{E}_{p_4} \cdot \mathbf{E}_{p_4}^* dA} \quad (7)$$



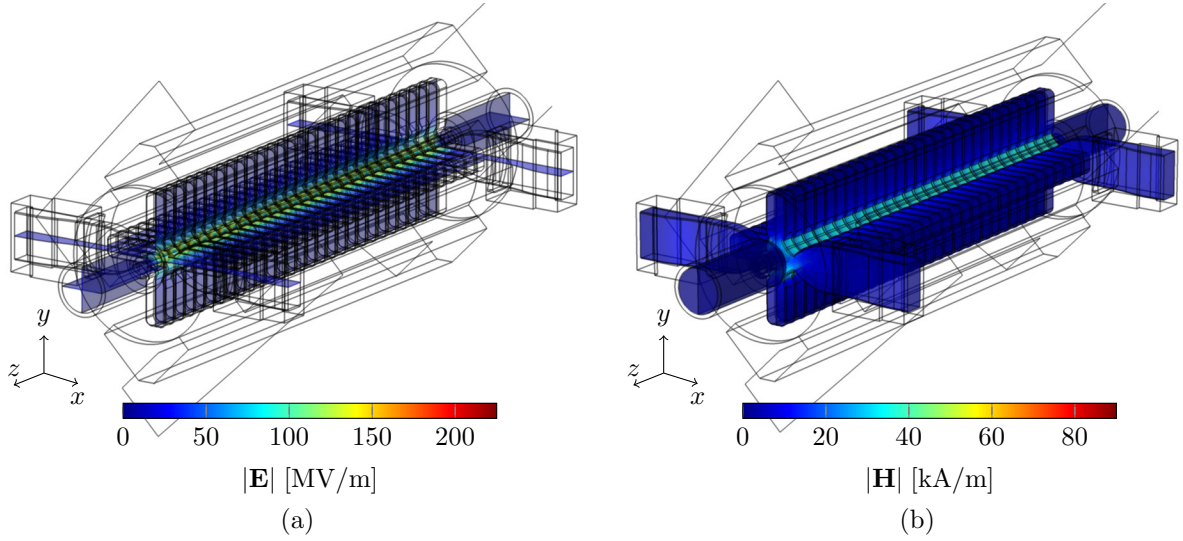


Figure 8: (a) Electric field intensity at the symmetry planes given by the traveling wave at nominal peak power of 43 MW at the input ports. (b) Magnetic field intensity at the inner surface of the structure as measured by an averaged input power of 1000 W.

Here,  $s_{11}$  is the RF reflection from both input ports combined while  $s_{21}$  is the RF transmission from both input ports to both output ports. Furthermore,  $\mathbf{E}$  is the total electric field intensity which solves (1) and  $\mathbf{E}_{pi}$  is the specific eigenmode solution satisfying (2) on the boundary of port  $i$ . Note, the concatenated consideration of input ports is necessary in order to satisfy the definition of scattering parameters, that is, one port is excited while the remaining ports are matched. As the electromagnetic field inside the structure is simultaneously excited by two ports it is not possible to evaluate for example the reflection for only port 1. However, the concatenated evaluation of the reflection for port 1 and 2 according to (6) is valid. Note, definitions (6) and (7) correspond to the scattering parameter of the symmetric case in Fig. 7(b), with only one port being excited. A second input port is implicitly given by the symmetry condition as it mirrors the first input port.

With integral operators defined on each port cross section, the evaluation of scattering parameters according to (6) can be implemented in COMSOL as follows:

```

S11 = (iintPort1((emw.Ex-emw.tEmodex_1)*conj(emw.tEmodex_1)
+ (emw.Ey-emw.tEmodey_1)*conj(emw.tEmodey_1)
+ (emw.Ez-emw.tEmodez_1)*conj(emw.tEmodez_1))
+ iintPort2((emw.Ex - emw.tEmodex_2)*conj(emw.tEmodex_2)
+ (emw.Ey-emw.tEmodey_2)*conj(emw.tEmodey_2)
+ (emw.Ez-emw.tEmodez_2)*conj(emw.tEmodez_2)))
/ (iintPort1(emw.tEmodex_1*conj(emw.tEmodex_1)
+ emw.tEmodey_1*conj(emw.tEmodey_1)
+ emw.tEmodez_1*conj(emw.tEmodez_1))
+ iintPort2(emw.tEmodex_2*conj(emw.tEmodex_2)
+ emw.tEmodey_2*conj(emw.tEmodey_2)
+ emw.tEmodez_2*conj(emw.tEmodez_2)))

```

The electromagnetic wave module `emw` provides direct access to all previously mentioned RF quantities. The surface integral operator defined on the port boundary  $n$  is denoted as `iintPortn()`. A detailed description of the integral operators in COMSOL is given in [6].

Using the method of periodic voltage standing-wave ratio described by Kroll et. al. [7]

the cell-to-cell phase advance and internal reflection calculate as

$$\psi_{\text{unit}}(z) = \arccos \frac{\Delta^+(z)}{2} \quad (8)$$

$$\Gamma_{\text{unit}}(z) = \frac{2 \sin \psi_{\text{unit}}(z) - j\Delta^-(z)}{2 \sin \psi_{\text{unit}}(z) + j\Delta^-(z)} \quad (9)$$

with the quantities  $\Delta^\pm(z)$  being superposed terms of the longitudinal electric field at the beam center, defines as

$$\Delta^\pm(z) = \frac{E_z(z + L_{\text{unit}}) \pm E_z(z - L_{\text{unit}})}{E_z(z)}. \quad (10)$$

Here,  $L_{\text{unit}}$  refers to the cell or unit length, which is about 8.332 mm for the TD26\_R05 design. By using the spatial `at3()` operator of COMSOL, which provides field components at arbitrary coordinates, the cell-to-cell phase advance along the beam axis can be evaluated as follows:

```
Phadvu = 180/pi*acos((at3(0,0,z+UnitLength, emw.Ez) + at3(0,0,z-UnitLength, emw.Ez))
/ at3(0,0,z, emw.Ez) / 2)
```

Both, the cell-to-cell phase advance and internal reflection based on the periodic voltage standing wave ratio are used to adjust the matching cells in the design phase. It is, thus of particular interest to study the impact of thermal expansion and contraction on these quantities along the center axis. Fig. 9(a) and (b) show respectively the cell-to-cell phase advance and internal reflection for each individual structure of the considered prototype assemblies. Despite of the common RF design, the phase advance of the TD26\_R05\_CC prototype assembly is slightly below 120 deg. This is due to the waveguides being shortened and rounded as shown in Fig. 3. Likewise the internal reflection is slightly higher than for the structures in the TD26\_R05\_SS prototype assembly.

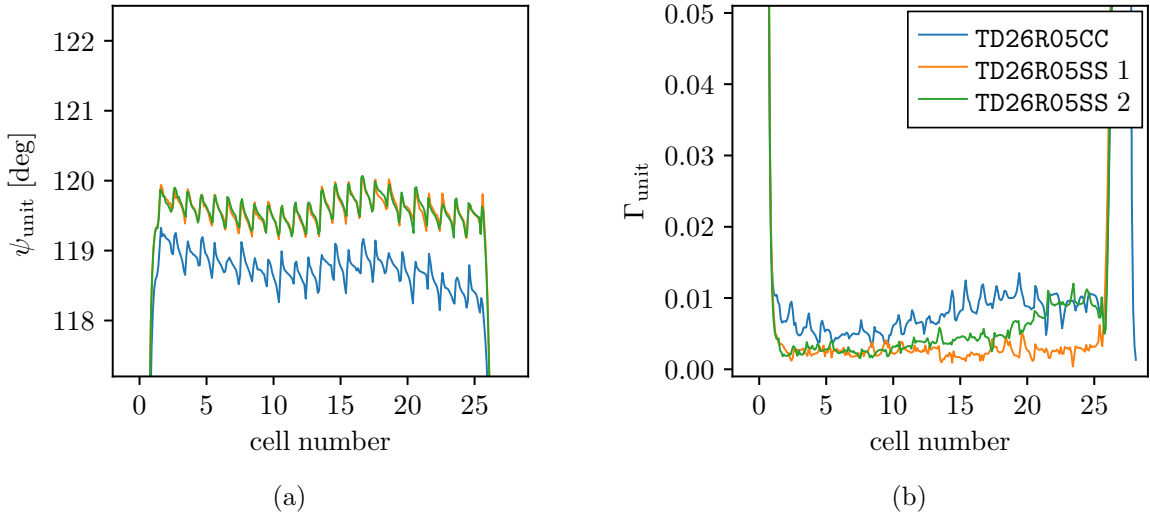


Figure 9: (a) The cell-to-cell phase advance and (b) internal reflection for different prototype assemblies. The quantities are derived from the periodic voltage standing wave method [7].



Traveling wave structures are further characterized by the stored energy per unit length,  $\mathcal{U}$ , dissipated power per unit length,  $P_{\text{diss}}$ , and the power flow through the structure cross section,  $P$ . Like the previously introduced cell-to-cell phase advance and internal reflection, all these quantities are functions of the longitudinal coordinate  $z$ , and are specified by the unit length, hence, the distance from cell to cell as illustrated in Fig. 6(b). Let  $h$  be a rectangular functions defined as

$$h(z) = \begin{cases} 1/L_{\text{unit}}, & 0 \leq z \leq L_{\text{unit}}, \\ 0, & \text{otherwise.} \end{cases} \quad (11)$$

and  $\delta$  be the delta distribution, the following relations apply for the stored energy, dissipated power, and power flow, respectively

$$\mathcal{U}(z) = \frac{\varepsilon_0}{2} \iiint_{\Omega_{\text{vac}}} h(z-z') \mathbf{E}(\mathbf{r}') \mathbf{E}^*(\mathbf{r}') dV', \quad \mathbf{r}' \in \Omega_{\text{vac}}, \quad (12)$$

$$P_{\text{diss}}(z) = \frac{1}{2} \Re\{Z_s\} \iint_{\partial\Omega_{\text{vac}}} h(z-z') \mathbf{H}(\mathbf{r}') \mathbf{H}^*(\mathbf{r}') dA', \quad \mathbf{r}' \in \partial\Omega_{\text{vac}}, \quad (13)$$

$$P(z) = \frac{1}{2} \iiint_{\Omega_{\text{vac}}} \delta(z-z') \mathbf{E}(\mathbf{r}') \times \mathbf{H}^*(\mathbf{r}') dV', \quad \mathbf{r}' \in \Omega_{\text{vac}}. \quad (14)$$

The first two integrals can be directly evaluated in COMSOL using the time averaged energy of the electromagnetic wave `emw.Wav` and the surface loss density `emw.Qsh` according to

```
intWavu = iintVacuum(h((dest(z)-z)/UnitLength)*emw.Wav)/UnitLength
intQshu = iintVacuum(h((dest(z)-z)/UnitLength)*emw.Qsh)/UnitLength
```

The operator `dest()` allows to exclude a variable from the integration, hence to distinguish between  $z$  and  $z'$  in (12)–(14). Fig. 10(a) and (b) show the stored energy and dissipated power per unit length, respectively, for the TD26\_R05 design with marginal differences between the prototype assemblies. It is worth noting that the use of a rectangular function according

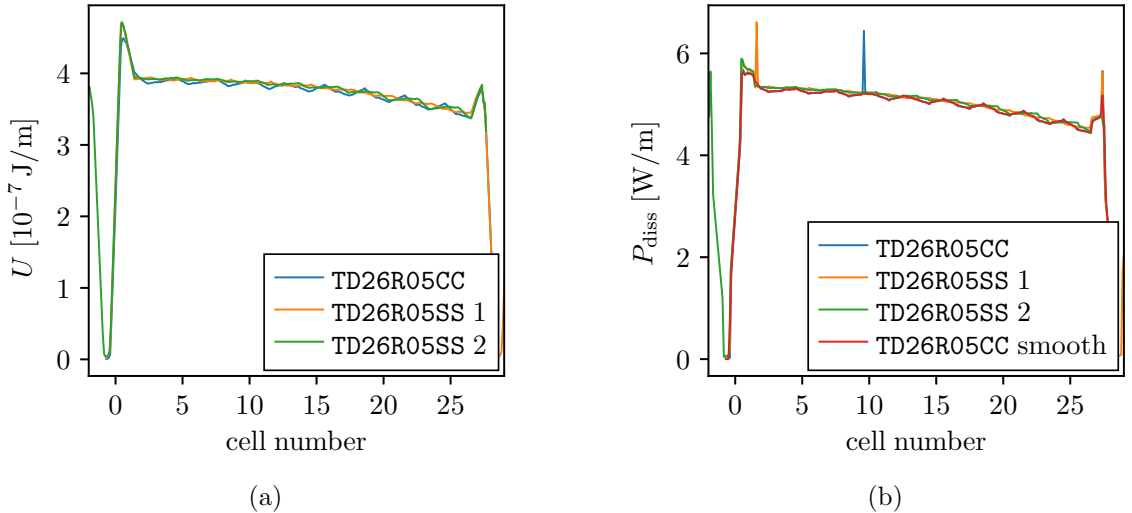


Figure 10: (a) Stored energy per unit length and (b) dissipated power per unit length for different prototype assemblies. An average power of 1 W at each input port is assumed.

to (11) provokes numerical noise due to its discontinuous character. This becomes particularly apparent for the dissipated power by several spikes as depicted in Fig. 10(b). In order to suppress such numerical fragments a slightly smoothed rectangular function in contrast to (11) can be used.

The power flowing through the cross section of the structure is easiest evaluated by a projection of the Poynting vector from the entire domain onto the  $yz$ -plane and further projected on the  $z$ -axis as sketched in Fig. 11. Note, this approach which equals an integration of the Poynting vector in the transverse  $xy$ -plane for each  $z$  along the structure, is numerically favorable and much more accurate than solving the volume integral in (14) due to the discontinuous character of the delta distribution. Note, the step-wise projection from the three-dimensional Poynting vector to the one-dimensional power flow by using an intermediate projection onto the  $yz$ -plane is for implementation reasons, only. The projection operators provided by COMSOL reduce the dimension by one when mapping a desired field quantity [8]. Once the projection operators are defined the power flow in longitudinal direction is calculated by a concatenated use according to

```
intPoavz = projZ(projYZ(emw.Poavz))
```

with `emw.Poavz` being the time averaged local power flow in  $z$ -direction. Fig. 12(a) shows the power flow through the structure cross section for the different prototype assemblies. The resulting profiles are approximately the same for all accelerating structures of the considered prototype assemblies. However, there is a slight difference with respect to the power flow through the first matching cell.

Further important quantity are the intrinsic quality factor  $Q$  defined as the ratio of stored energy per unit length and corresponding energy dissipated in the cavity wall over one RF cycle according to

$$Q(z) = \frac{\omega \mathcal{U}(z)}{P_{\text{diss}}(z)}, \quad (15)$$

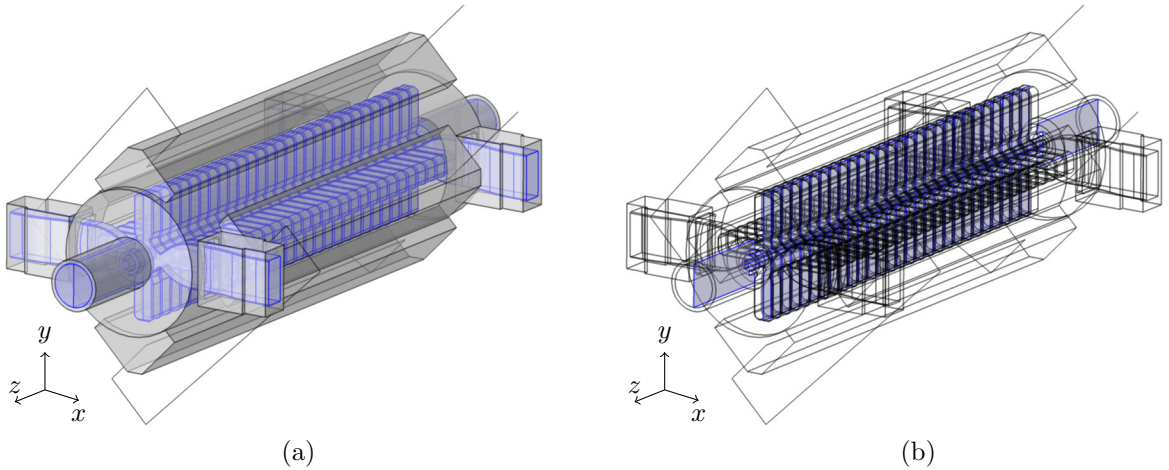


Figure 11: Projection of an arbitrary field quantity defined in the inner volume filled with vacuum (a) onto the  $yz$ -plane (b). This approach is used to evaluate the power flow through the cross section of the structure as it requires the integration of the Poynting vector in the transverse plane for each  $z$ .

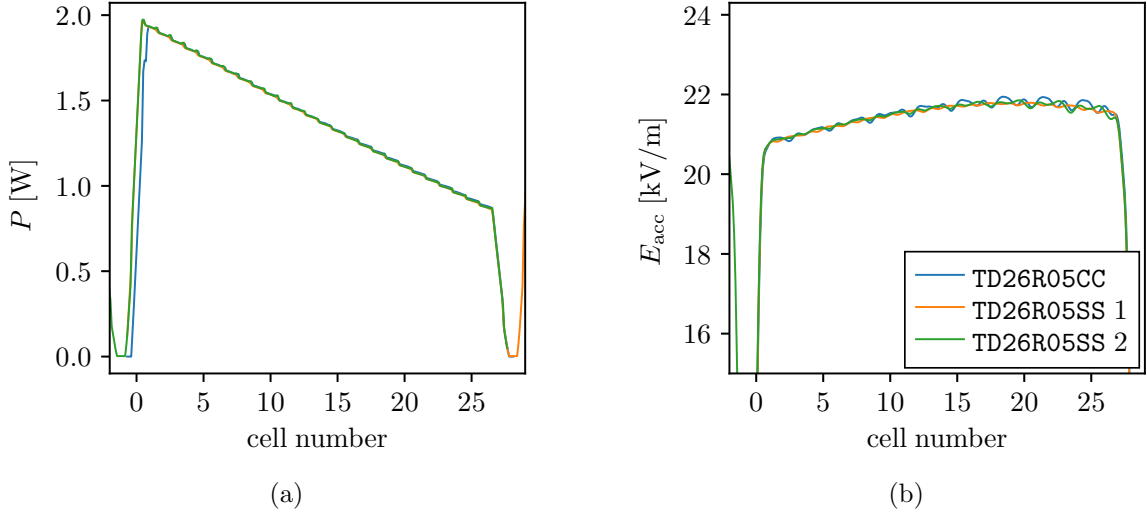


Figure 12: (a) Power flow through the structure cross section. (b) Longitudinal RF voltage per unit length on the center axis. An average power of 1 W at each input port is assumed.

the group velocity  $v_g$  which is the speed at which RF power propagates through the traveling wave structure, given by

$$v_g(z) = \frac{d\omega}{dk} = \frac{P(z)}{\mathcal{U}(z)}, \quad (16)$$

and the filling time  $t_{\text{fill}}$  defined as

$$t_{\text{fill}} = \int_0^L \frac{dz}{v_g(z)}. \quad (17)$$

The longitudinal RF voltage per unit length on the beam axis  $\Omega_{\text{beam}}$  is defined by the integral of the longitudinal electric field component taking into account the phase advance for a particle at the speed of light, and is given by

$$E_{\text{acc}}(z) = \left| \int_{-\infty}^{\infty} h(z-z') \mathbf{E}(\mathbf{r}') e^{jk_0 z'} \mathbf{e}_z dz' \right|, \quad \mathbf{r}' \in \Omega_{\text{beam}} \quad (18)$$

Note, this quantity corresponds to the accelerating gradient in case of unloaded standing wave structures. Moreover, the shunt resistance  $R_{\text{sh}}$  and geometric shunt resistance  $(R/Q)$  are calculated from the longitudinal voltage gradient respectively as

$$R_{\text{sh}}(z) = \frac{E_{\text{acc}}^2(z)}{P_{\text{diss}}(z)} \quad (19)$$

$$(R/Q)(z) = \frac{E_{\text{acc}}^2(z)}{\omega \mathcal{U}(z)} \quad (20)$$

Finally, the accelerating gradient of unloaded traveling wave structures is given by [9]

$$\tilde{E}_{\text{acc}}(z) = E_{\text{acc}}(0) \sqrt{\frac{v_g(0)}{v_g(z)}} \sqrt{\frac{(R/Q)(z)}{(R/Q)(0)}} \exp\left(\frac{\omega}{2} \int_0^z \frac{dz'}{v_g(z')Q(z')}\right). \quad (21)$$

In order to reduce post processing time, it is recommendable to export only the stored energy  $\mathcal{U}$ , dissipated power  $P_{\text{diss}}$ , and longitudinal voltage  $E_{\text{acc}}$  each per unit length as well as the power flow through the structure cross section,  $P$ . The remaining quantities can be subsequently derived without re-calculating the integrals of (12)–(14) and (18).

### 3.2 Heat Transfer and Pipe Flow

The heat transfer in the structure is characterized by the inward heat flux which corresponds to the RF losses as discussed in Sec. 3.1, the convection through cooling channels, and eventual heat dissipation to air. The minor but not negligible contribution of the latter one is difficult to quantify by simulations as it depends on the complex ventilation system of the tunnel. Figs 13(a) and (b) shows respectively the total heat deposit of the RF field as well as heat dissipation into air for various case scenarios of the TD26\_R05\_CC prototype assembly.

The momentum and mass conservation of the one-dimensional flow in circular cooling channels of diameter  $d$  and cross section area  $A$  are given by

$$d \nabla p + f_D \frac{\rho}{2} \mathbf{u} |\mathbf{u}| = 0, \quad (22)$$

$$\nabla \cdot (p A \mathbf{u}) = 0, \quad \mathbf{r} \in \Omega_{\text{pipe}}, \quad (23)$$

with the cross section averaged fluid velocity  $\mathbf{u}$  and pressure  $p$  being solved for. Both quantities are defined along the one-dimensional domain of the cooling path  $\Omega_{\text{pipe}}$ . The second term in (22) accounts for surface shear stresses [10, p. 340]. The friction factor  $f_D$ ,

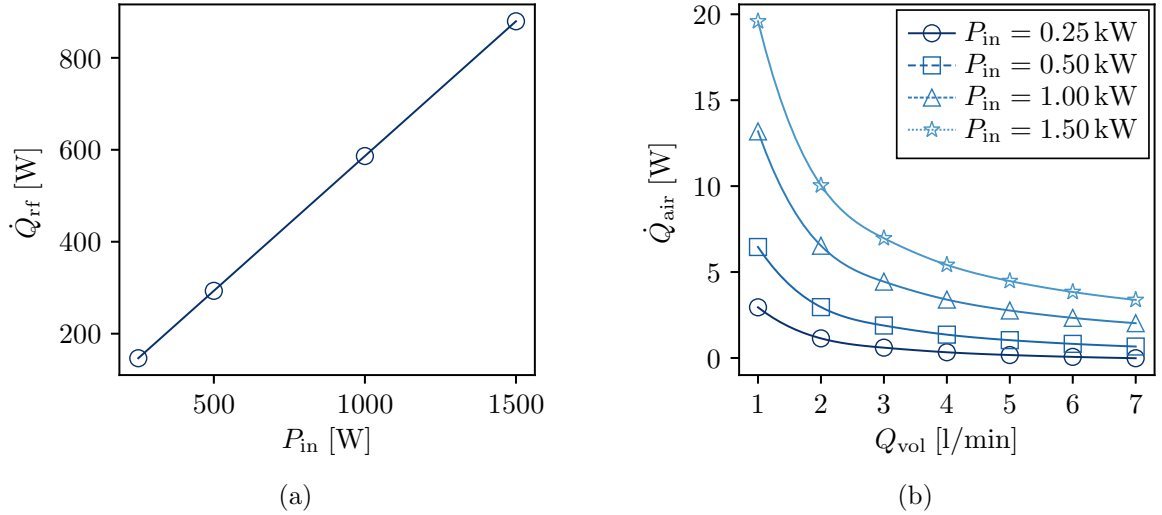


Figure 13: (a) Time averaged RF power dissipated into the total cavity wall of the TD26\_R05\_CC prototype assembly as a function of inserted RF power at both input ports. (b) Corresponding heat dissipation into air assuming different flow rates through the single cooling circuit as illustrated in Fig. 3(a). A fixed heat transfer coefficient of  $5 \text{ W}/(\text{m}^2\text{K})$  accounts for the surrounding air convection.

also denoted as Darcy friction factor, strongly depends on the flow regime as expressed by the Reynolds number:

$$\text{Re} = \frac{\rho|\mathbf{u}|d}{\mu}. \quad (24)$$

The friction factor of a fully developed laminar flow ( $\text{Re} \lesssim 2300$ ) is given by

$$f_D = \frac{64}{\text{Re}}. \quad (25)$$

Turbulent flows may further depend on the relative surface roughness  $\epsilon/d$  of the pipe. Both dependencies are implicitly correlated in the phenomenological Colebrook–White equation which is illustrated in Fig. 14 for a wide range of the Reynolds number and varying roughness. The Moody chart provides a convenient way to estimate the pressure drop needed to sustain

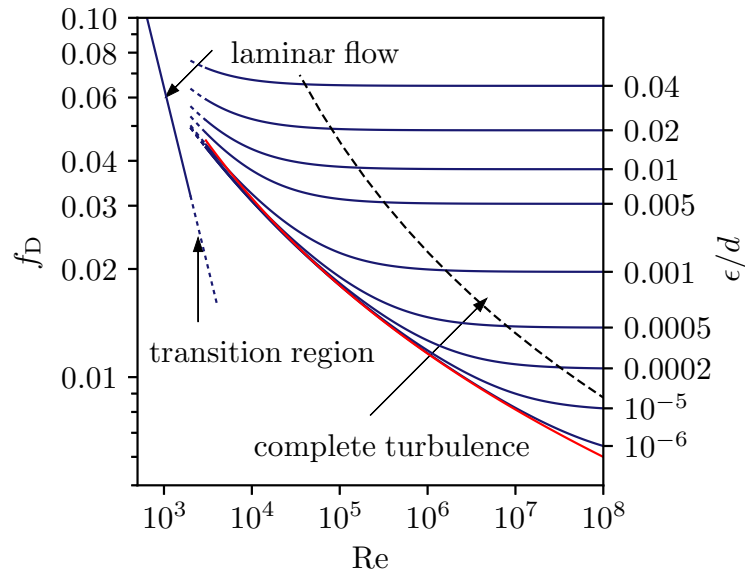


Figure 14: Moody diagram providing the friction factor  $f_D$  as a function of Reynolds number  $\text{Re}$ , with the relative roughness  $\epsilon/d$  being varied. The onset of complete turbulence is approximately at 1% above the corresponding friction factor for infinite Reynolds number. In red, the approximation for smooth pipes after Petukhov according to (27).

an internal flow  $u_0$  over the length  $L$  which follows from (22) according to

$$\Delta p = -f_D \frac{L \rho u_0^2}{d}. \quad (26)$$

Various approximations of the Colebrook–White equation have been developed over the past decades in order to express the friction factor in an explicit manner. A single correlation encompassing Reynolds numbers from  $3 \times 10^3$  to  $5 \times 10^6$  is given by [11]

$$f_D = (0.79 \ln \text{Re} - 1.64)^{-2}. \quad (27)$$

It applies to smooth pipes whose roughness is completely covered by a viscous layer. Note, this case corresponds to the highlighted curve in Fig. 14. Another approximation developed

by Churchill [12] applies to all flow regimes including the laminar flow, and is used for the present simulations to evaluate the friction factor locally. If not other stated a surface roughness of  $\epsilon = 0.0015$  mm is considered for the simulations, which applies to drawn tubes [10, p. 443]. Note, the cooling pipes within traveling wave structures are drilled yielding, in general, higher surface roughness and, thus, larger friction.

The energy conservation of the coolant and surrounding structure can be described as

$$c_p \rho A \mathbf{u} \nabla T = \nabla \cdot (k_{\text{pipe}} A \nabla T) + f_D \frac{\rho A}{2d} |\mathbf{u}|^3 + \dot{Q}_{\text{wall}}, \quad \mathbf{r} \in \Omega_{\text{pipe}}, \quad (28)$$

$$0 = \nabla \cdot (k_{\text{solid}} \nabla T), \quad \mathbf{r} \in \Omega_{\text{solid}} \setminus \Omega_{\text{pipe}}, \quad (29)$$

where  $c_p$  is the heat capacity of the coolant at constant pressure and  $k$  is the thermal conductivity of the particular material. The terms on the right hand side of (28) account respectively for the conductive heat transfer, energy dissipation by internal friction, and heat exchange with the surrounding structure. The latter one is calculated according to

$$\dot{Q}_{\text{wall}} = h_{\text{pipe}} \pi d \Delta T, \quad (30)$$

with  $\Delta T$  being the temperature difference to the surrounding structure. The convection heat transfer coefficient  $h_{\text{pipe}}$  is calculated via the Nusselt number describing the enhancement of heat transfer through a fluid layer by convection relative to conduction according to

$$h = \text{Nu} \frac{k}{d} \quad (31)$$

Fig. 15 shows the Reynolds and Nusselt number obtained from thermal simulations of the TD26\_R05\_CC prototype assembly as sketched in Fig. 3(a), with varying RF power at the input

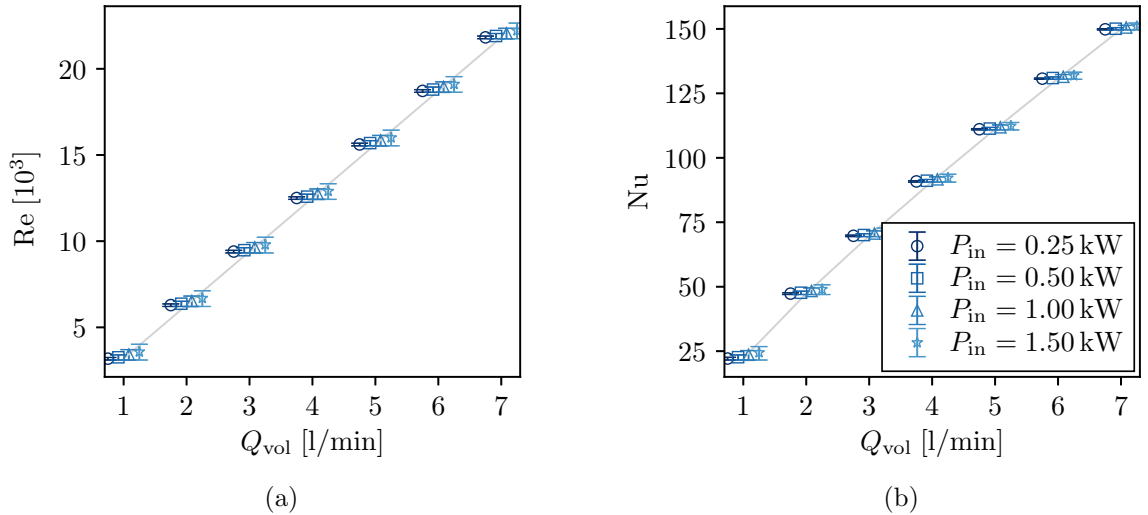


Figure 15: Thermal study of the TD26\_R05\_CC prototype assembly as sketched in Fig. 3(a), with varying RF power at the input ports and gradually increased flow velocity of water in the single cooling circuit. (a) The Reynolds and (b) Nusselt number, each averaged over the entire cooling path. The error bars result from the corresponding minimum and maximum.

ports and gradually increased flow velocity of water in the single cooling circuit. Note, the flow becomes close to be laminar at an average velocity of 11/min. Though, the convection provided by the cooling channels generally varies along the flow direction, average values appear fairly accurate in the present cases.

For laminar flow in circular pipes an analytic solution of the Nusselt number can be derived which gives

$$\text{Nu} = 3.66. \quad (32)$$

The Nusselt number for turbulent flow is given by Gnielinski according to [10, p. 441]

$$\text{Nu} = \frac{(f_D/8)(\text{Re} - 1000)\text{Pr}}{1 + 12.7(f_D/8)^{1/2}(\text{Pr}^{2/3} - 1)}, \quad (33)$$

which is valid in the range of  $0.5 \lesssim \text{Pr} \lesssim 2000$  and  $3 \times 10^3 \lesssim \text{Re} \lesssim 5 \times 10^6$ . The Prandtl number  $\text{Pr}$  is defined by the heat capacity  $c_p$ , viscosity  $\mu$  and thermal conductivity  $k$  as

$$\text{Pr} = \frac{c_p \mu}{k}. \quad (34)$$

The problem (28)–(29) further requires boundary conditions in order to involve the RF heat source and power dissipation to air. They are given by the following two equations

$$\mathbf{n} \cdot (k_{\text{solid}} \nabla T) = \frac{1}{2} \Re\{Z_s\} |\mathbf{H}|^2, \quad \mathbf{r} \in \partial\Omega_{\text{solid}} \cap \partial\Omega_{\text{vac}}, \quad (35)$$

$$\mathbf{n} \cdot (k_{\text{solid}} \nabla T) = h_{\text{air}}(T - T_{\text{amb}}), \quad \mathbf{r} \in \partial\Omega_{\text{solid}} \setminus \partial\Omega_{\text{vac}}, \quad (36)$$

where  $\mathbf{H}$  is the magnetic field intensity at the common boundary between solid and vacuum domain,  $Z_s$  is the frequency and material dependent surface impedance according to Sec. 3.1,  $T_{\text{amb}}$  is the ambient temperature, and  $h_{\text{air}}$  represents the convection heat transfer coefficient provided by the environmental air. The right hand side of (36) may be extended by heat radiation. The corresponding heat flux contribution  $\dot{\mathbf{q}}_{\text{rad}}$  is given as

$$\mathbf{n} \cdot \dot{\mathbf{q}}_{\text{rad}} = \varepsilon \sigma (T^4 - T_{\text{amb}}^4), \quad \mathbf{r} \in \partial\Omega_{\text{solid}} \setminus \partial\Omega_{\text{vac}}, \quad (37)$$

with the material specific emissivity factor  $\varepsilon$  and Stefan-Boltzmann  $\sigma$ . The first one was measured to be 0.05 [13]. Despite of its marginal impact on the thermal behavior of the structure, the heat radiation is accounted in all subsequent studies. A detailed tutorial for simulating self consistently the heat transfer in solids combined with one-dimensional flows using COMSOL is provided in [14].

Figs. 16 and 17 show the temperature distribution within the solid and cooling pipes of the considered prototype assemblies. An averaged RF power of 1 kW per accelerating structure is applied at the particular input ports. Based on the results of [13], the ambient and water inlet temperatures were chosen to be 28 degC and 27 degC, respectively, while the air convective heat transfer coefficient is 5 W/(m<sup>2</sup>K). Note, the latter one generally varies over the surface as the heat transfer depends on the local air flow. The studies in [13] suggest values between 5 W/(m<sup>2</sup>K) to 15 W/(m<sup>2</sup>K) depending on the tunnel ventilation system. Furthermore, an average water flows of 31/min through the individual single cooling circuit is assumed. In subsequent studies, this quantity is varied. Note, the Xbox test stands are



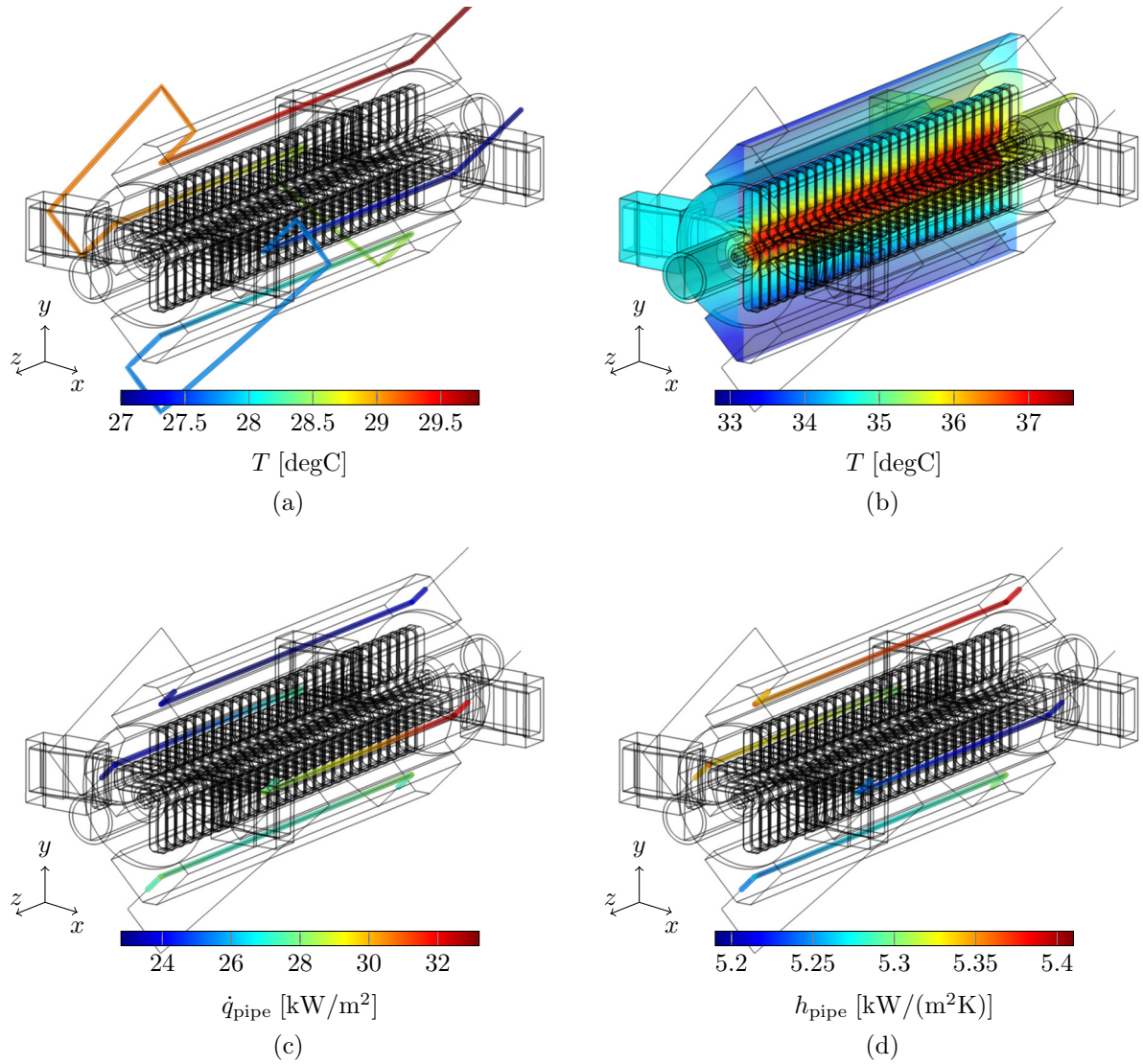


Figure 16: Thermal study of the TD26\_R05\_CC prototype assembly, with the input RF power, water flow rate, and air convective heat transfer coefficient being 1 kW, 31/min and 5 W/(m<sup>2</sup>K), respectively. Temperature profile (a) of the coolant and (b) within the solid. (c) Heat flux and (d) heat transfer coefficient between water and solid.

equipped with chillers providing a flow rate of approximately 71/min. While this amount ensure stable thermal conditions during the high-power tests and structure conditioning, for operation, it is too high and unfavorable with regard to cavitation.

Despite of the high thermal conductivity of copper, the heat is very much localized around the irises as illustrated in Figs. 16(b) and 17(b). The traveling wave structures of the TD26\_R05\_SS prototype assembly are cooled in series causing different temperature levels. Given the simulated heat exchange  $\dot{Q}_{\text{wall}}$  and temperature difference  $\Delta T$  between water and surrounding solid, the corresponding heat flux and heat transfer coefficient can be derived from (30). The implementation in COMSOL is as:

```
qpipe = nipfl.Qwall/(pi*Pipe_Diameter)
```



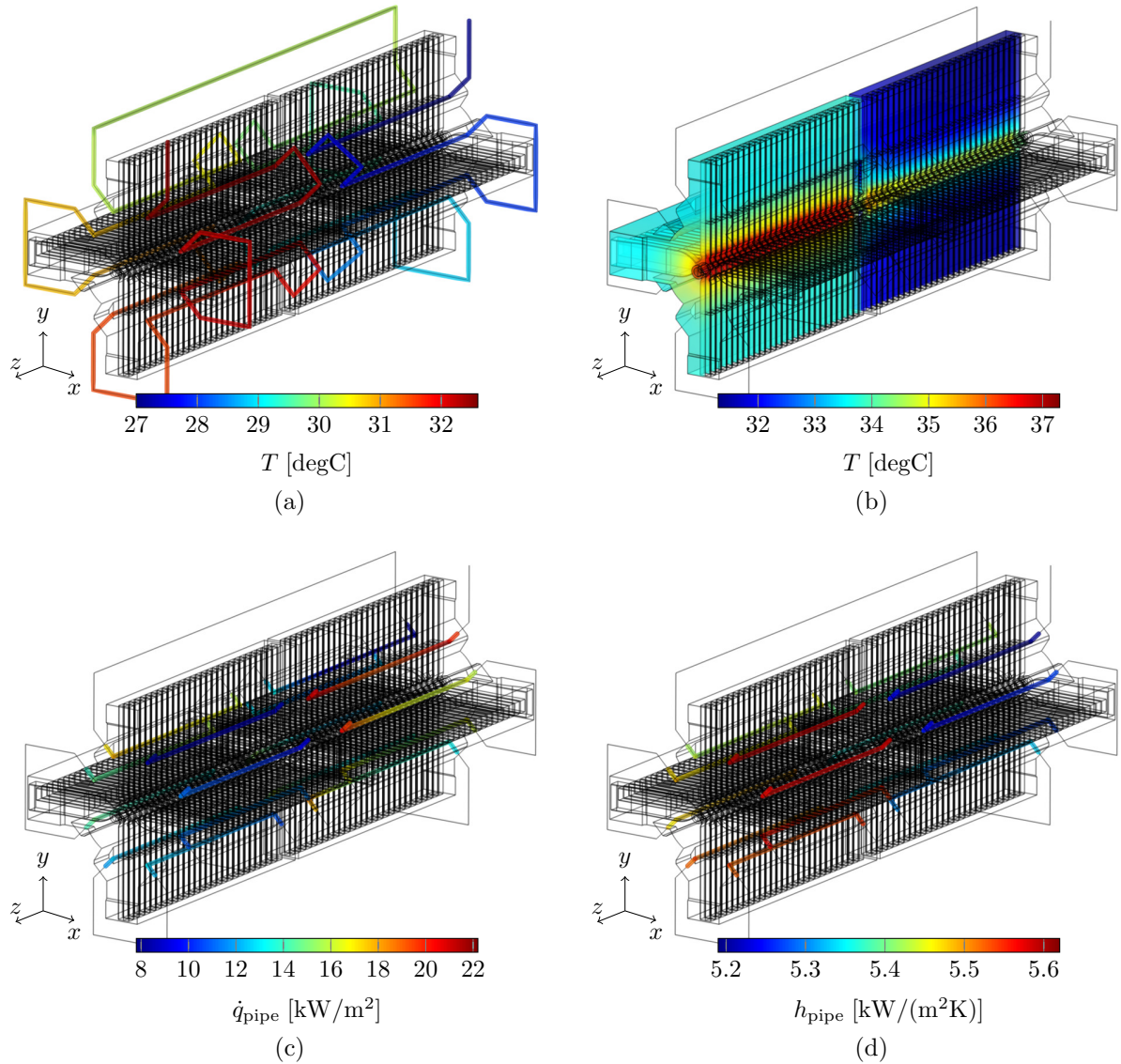


Figure 17: Thermal study of the TD26\_R05\_SS prototype assembly, with the input RF power, water flow rate, and air convective heat transfer coefficient being 1 kW, 31/min and 5 W/(m<sup>2</sup>K), respectively. Temperature profile (a) of the coolant and (b) within the solid. (c) Heat flux and (d) heat transfer coefficient between water and solid.

$$h_{\text{pipe}} = q_{\text{pipe}} / (\text{nipfl.Text} - T2)$$

Here, `nipfl` refers to the non-isothermal pipe flow module which provides the variables `T2` and `Text` being the local temperature of the fluid and surrounding solid, respectively. It further provides access to the heat exchange per length `Qwall`.

The convection heat transfer coefficient of the water only slightly varies over the cooling path as depicted in Figs. 16(d) and 17(d). For the sake of simplicity, it can be assumed constant, an approach which is typically used, for instance, using ANSYS, with the heat transfer coefficient being estimated from (31) and (33) assuming a constant average flow, thus, constant Reynolds number according to (24), as well as the smooth pipe approximation

of (27) to derive the friction factor  $f_D$ . These assumptions are in particular valid towards larger flow rates and smaller input RF power as indicated in Fig. 15. However, even for an input RF power of 1.5 kW and a flow rate of 1 l/min which is close to the transition from turbulent to laminar flow, the Nusselt number varies by approximately 20%, only. In the presence of higher surface roughness the error of the smooth pipe approximation (27) may become significant. Assuming a ten times rougher surface than provided by drawn tubes, hence  $\epsilon/d \sim 0.002$  mm, yield already a slight deviation from the smooth pipe approximation

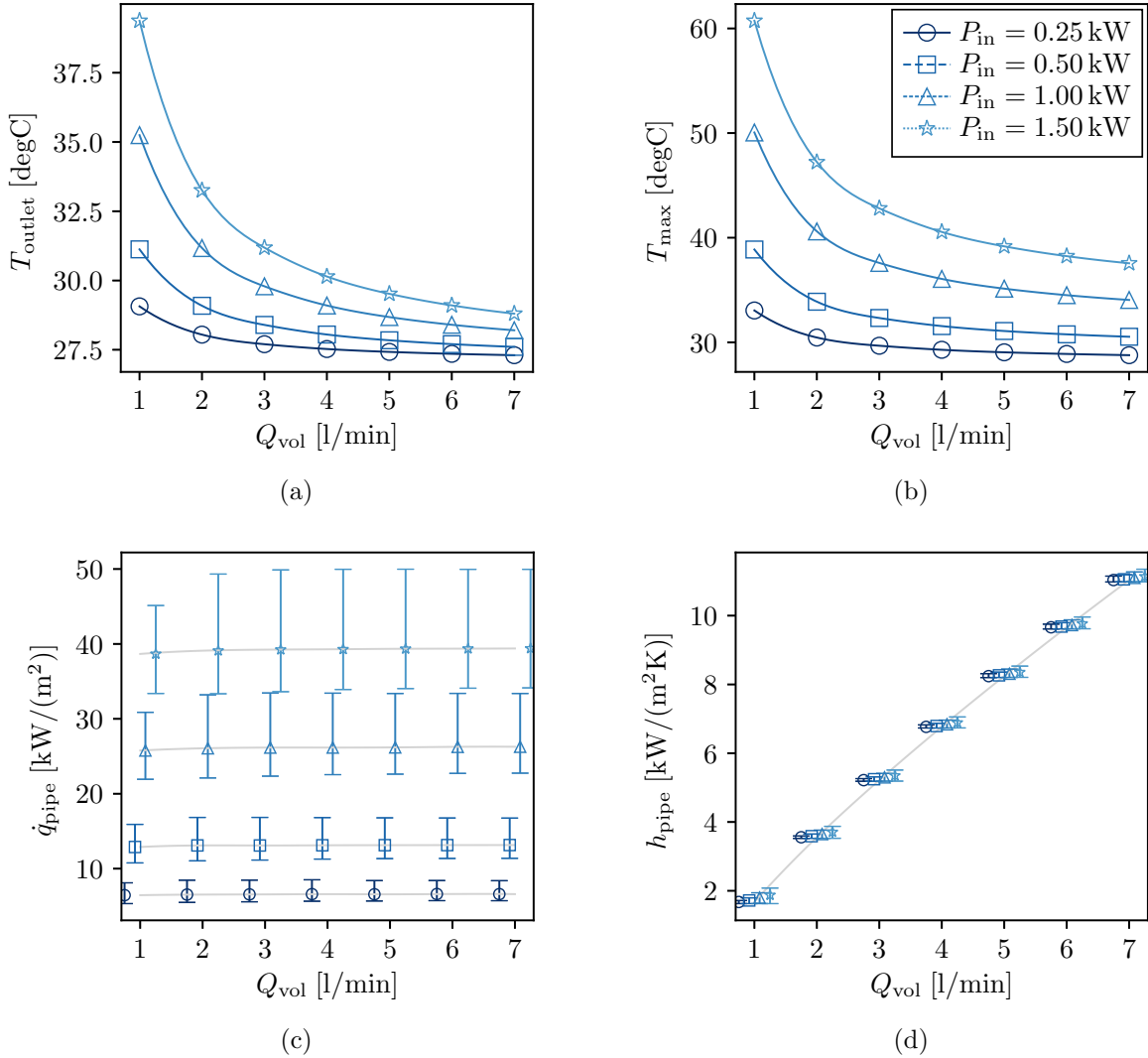


Figure 18: Thermal study of the TD26\_R05\_CC prototype assembly with varying RF input power and water flow rate. An ambient temperature of 28 degC is assumed while the water temperature at the inlet is 27 degC. (a) Water temperature at the outlet. (b) Maximum temperature provided by the structure. (c) heat flux between the coolant and surrounding solid. (d) Convection heat transfer coefficient provided by the coolant. The latter two quantities are averaged over the single cooling circuit, with error bars accounting for the corresponding minimum and maximum along the path.

at  $Re = 10^4$  as shown by the Moody diagram in Fig. 14. According to Fig. 15(a), this corresponds to a volume flow of 31/min.

Fig. 18 shows the thermal behavior of the TD26\_R05\_CC prototype assembly with varying input RF power and water flow rate. For an average RF power of 1.5 kW at the input ports, the temperature around the irises may rise by several tens of degree Celsius. Starting from a flow rate of 31/min the temperature rise becomes saturated. It is, thus not efficient and with respect to cavitation phenomena even unfavorable to increase the flow rate more than 41/min or 51/min. In order to overcome this drastic temperature increase at relatively

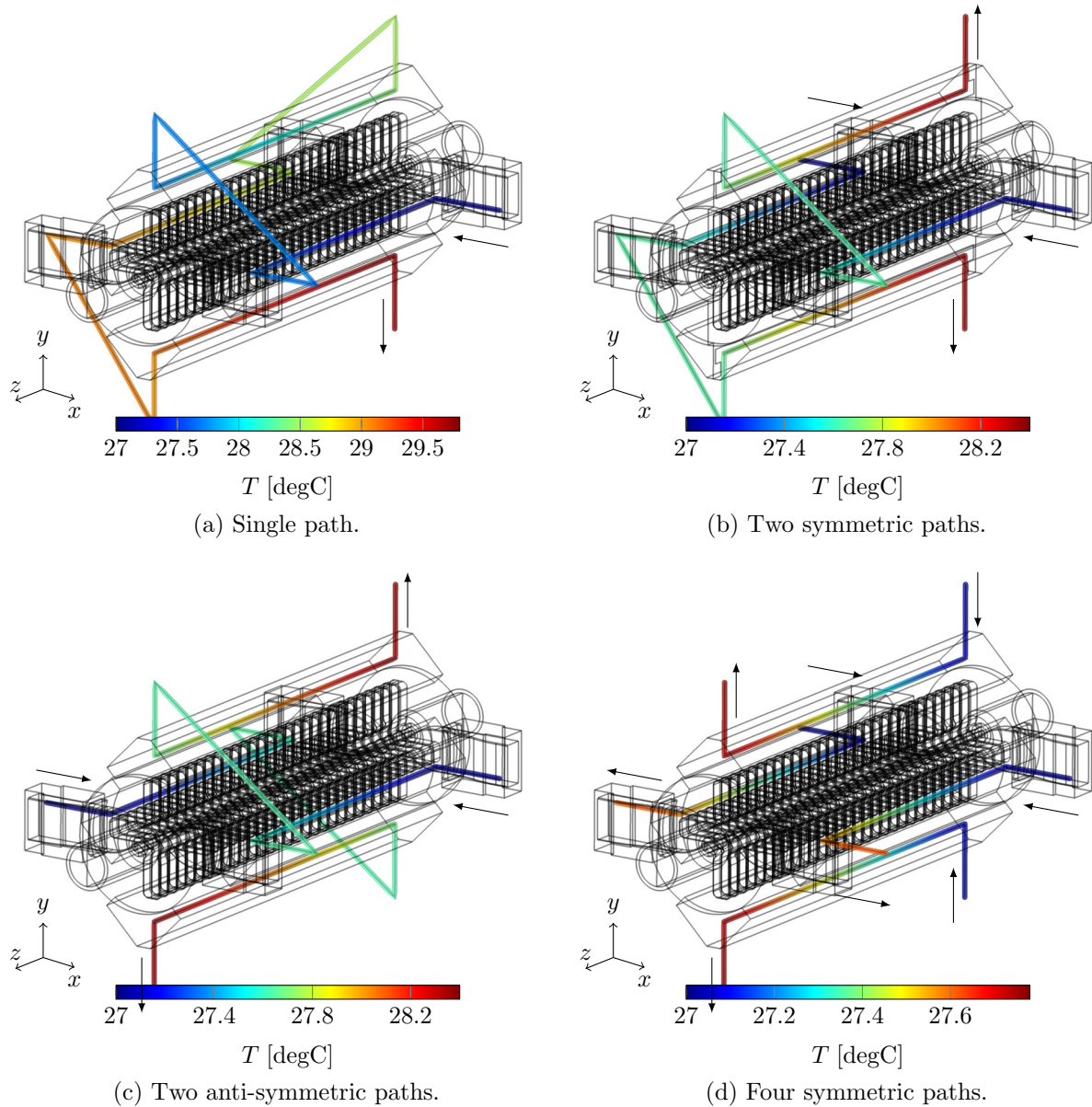


Figure 19: Temperature distribution of the coolant along various paths applied on the TD26\_R05\_CC assembly, with the input RF power, water flow rate, and air convective heat transfer coefficient being 1 kW, 31/min and  $5 \text{ W}/(\text{m}^2\text{K})$ , respectively.

high average RF power, the cooling system must be located closer to the irises. This has been achieved for the CLIC-G structures by providing the disks with dedicated holes for the cooling circuits. The convection heat transfer coefficient varies linearly with the flow rate and is approximately constant along the cooling path for all considered cases. The corresponding heat dissipated into the environmental air is shown in Fig. 13(b) in the beginning of this section. Its contribution is marginal in comparison to the heat evacuated by the coolant which amounts roughly 98 % of the RF power dissipated in the structure wall [Fig. 13(a)].

Furthermore, the thermal behavior of the TD26\_R05\_CC prototype assembly was studied for different cooling paths as illustrated in Fig. 19. Besides the original single circuit providing a back and forth flow through the individual cooling blocks, two symmetric and anti-symmetric, as well as four symmetric paths are considered. Note for comparison, the total flow is preserved. Hence, the four paths in Fig. 19(d) share a flow rate of 3 l/min while in Fig. 19(a), the same total flow is applied to a single path. A comparison of the four circuits by means of water outlet temperature and peak temperature in the structure, both with varying flow rate, are depicted in Fig. (a) and (b), respectively. The average input RF power is set to 1 kW. As previously, an ambient temperature of 28 degC is assumed while the water temperature at the inlets equals 27 degC. The air convective heat transfer coefficient is adjusted to 5 W/(m<sup>2</sup>K) based on the results of [13]. The outlet temperature is notably lowered by the use of parallel paths, however, the impact on temperature distribution within the solid is minor. For instance, the peak value at a flow rate of 3 l/min is approximately 1 degC lower in the presence of four symmetric paths than in the presence to the single path. Both cooling circuits comprising two symmetric and anti-symmetric paths do not show any notable difference in terms of the considered temperature. However, the differences will be notable for the displacement of the center axis along the structure due to thermal expansion

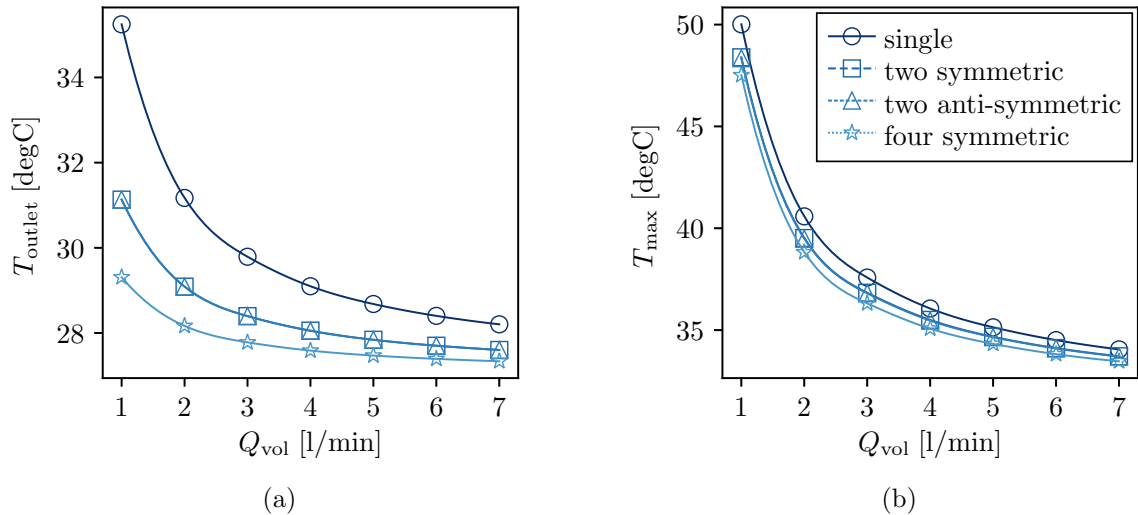


Figure 20: Thermal study of the TD26\_R05\_CC prototype assembly with different cooling paths according to Fig. 19. The input RF power and air convective heat transfer coefficient are 1 kW and 5 W/(m<sup>2</sup>K), respectively. An ambient temperature of 28 degC is assumed while the water temperature at the inlets is 27 degC. (a) Water temperature at the outlet. (b) Maximum temperature provided by the structure.

as considered in the following section.

Finally, the surface roughness of the original single cooling circuit was varied in order to investigate the impact of friction on the thermal behavior of the TD26\_R05\_CC prototype assembly. Figs. 21(a) and (b) show the peak temperature within the structure and convective water heat transfer coefficient, with the input RF power and water flow rate being 1000 W and 31/min, respectively. Based on the results of [13], the ambient and water inlet temperatures were chosen to be 28 degC and 27 degC, respectively, while the air convective heat transfer coefficient is 5 W/(m<sup>2</sup>K). The surface roughness ranges by two orders of magnitude from 1.5 μm provided by drawn tubes up to 160 μm were the smooth pipe approximation according to (27) is not valid anymore. Note, the water pipes are provided by drilled holes in the solid copper cooling blocks and may reveal much larger surface roughness than drawn tubes. In the considered range, the water convective heat transfer coefficient increases by approximately 50% while the maximum temperature within the solid only marginally reduces by 1.5 degC as depicted in Fig. 21. By comparing the results with Figs. 18(b) and (d), an increase of surface roughness from 1.5 μm to 150 μm with the flow rate being fixed at 31/min causes a similar effect on the thermal behavior of the structure as an increase of the water flow rate from 31/min to 41/min, with the surface roughness remaining at 1.5 μm.

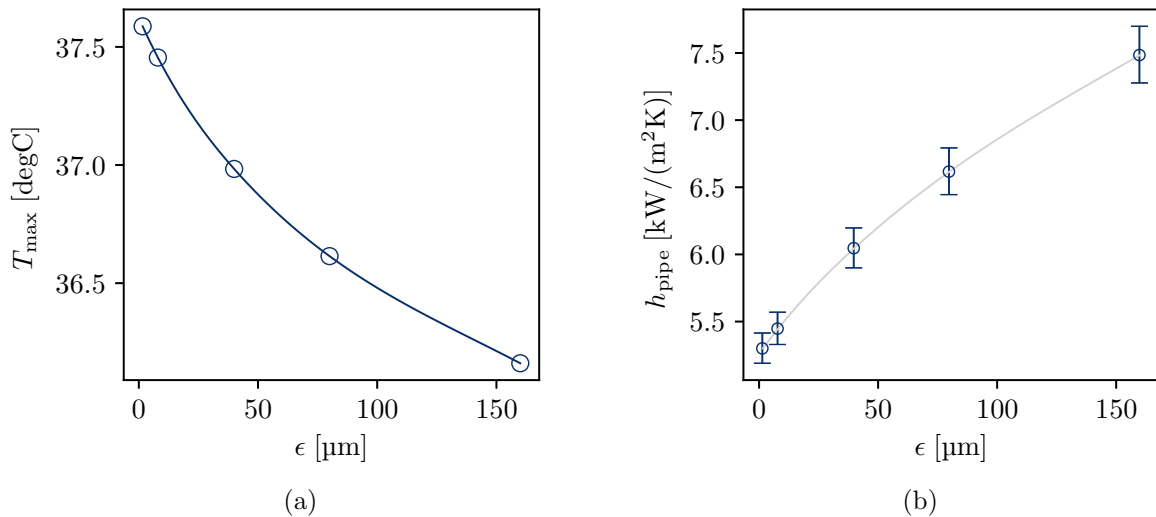


Figure 21: Thermal study of the TD26\_R05\_CC prototype assembly with varying surface roughness of the cooling pipes. The input RF power, water flow rate, and air convective heat transfer coefficient are 1000 W, 31/min, and 5 W/(m<sup>2</sup>K), respectively. An ambient temperature of 28 degC is assumed while the water inlet temperature is 27 degC. (a) Maximum temperature provided by the structure. (b) Convection heat transfer coefficient provided by the coolant. The latter one is averaged over the single cooling circuit, with error bars accounting for the minimum and maximum along the path.



### 3.3 Structural Deformation

The deformation of an isotropic linear elastic solid with the material specific Young's modulus  $E$ , Poisson ratio  $\nu$ , and density  $\rho$  can be described by Navier's equations according to [15]

$$\frac{E}{2(1+\nu)} \left( \frac{1}{1-2\nu} \nabla(\nabla \cdot \mathbf{u}) + \nabla^2 \mathbf{u} \right) + \mathbf{f} = \rho \frac{\partial^2 \mathbf{u}}{\partial t^2} \quad \mathbf{r} \in \Omega_{\text{solid}}, \quad (38)$$

where  $\mathbf{u}$  corresponds to the unknown displacement vector field. The force per unit volume due to thermal expansion is given by [16]

$$\mathbf{f} = -\frac{E}{3(1-2\nu)} \alpha_T \nabla T, \quad (39)$$

with  $\alpha_T$  as the temperature coefficient of linear thermal expansion. As in the previous section, only the stationary case shall be considered, that is the right hand side of (38) vanishes. Furthermore, a boundary condition must be added in order to allow for a unique solution. The structure is fixed on one end by forcing zero azimuthal and longitudinal displacement along the highlighted circular edges in Figs. 22(a) and (b) for the TD26\_R05\_CC or TD26\_R05\_SS prototype assembly, respectively. This particular constraints which are close to realistic conditions, ensure that the beam remains at the center when entering the structure and deviates from the center while propagating through the structure. Fig. 23 gives an indication of the center displacement taking into account the temperature distribution of Fig. 16(b). It shows the radial displacement in the  $xy$ -plane around but not in the axial center of the TD26\_R05\_CC prototype assembly since the inner volume filled with vacuum is not involved in the structural simulations. In order to evaluate the axial center displacement due to thermal expansion or contraction for each  $z$  along the structure, the components of transverse

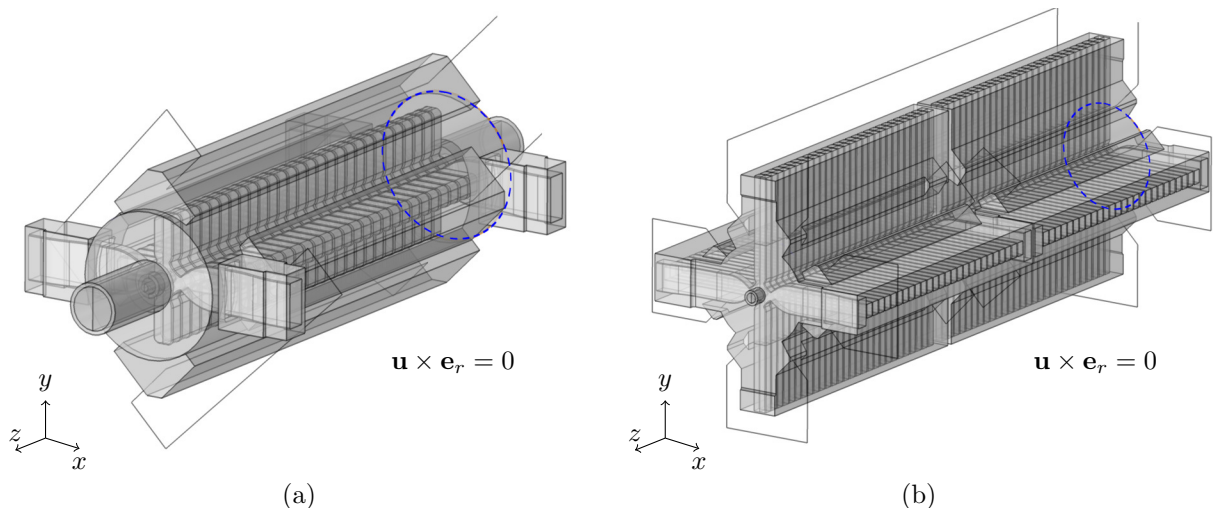


Figure 22: Boundary condition for the structural deformation due to thermal expansion. The structures are fixed on one end by forcing zero azimuthal and longitudinal displacement along the highlighted circular paths. (a) TD26\_R05\_CC and (b) TD26\_R05 prototype assembly.

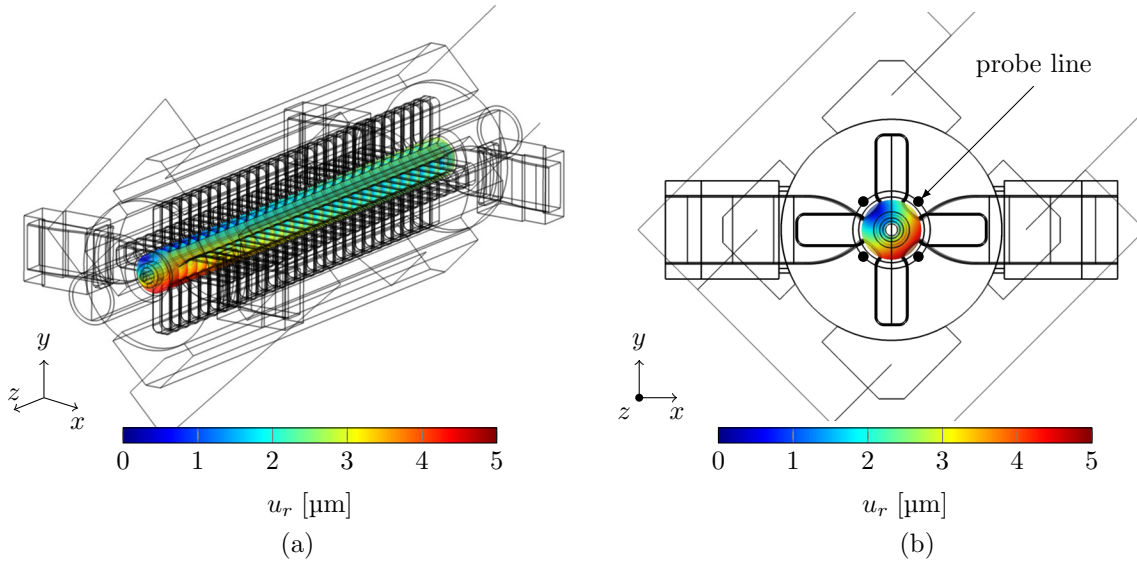


Figure 23: Radial deformation due to thermal expansion of the TD26\_R05\_CC assembly with single circuit cooling provided an input RF power, water flow rate, and air convective heat transfer coefficient of 1 kW, 31/min and 5 W/(m<sup>2</sup>K), respectively. An ambient temperature of 28 degC is assumed while the water temperature is set to 27 degC at the inlet. (a) Perspective view. (b) Cross-sectional view at the structure exit. The center axis displacement along the structure is measured by superposing the transverse displacements over four probe lines close to the irises and highlighted by the black dots.

displacement in  $x$ - and  $y$ -direction are averaged over four probe lines equally distributed on a cylinder barrel as sketched in the cross-sectional view of Fig. 23(b). By using the `at3()` command to evaluate an arbitrary quantity at specific three-dimensional coordinates, the evaluation of axial center displacement can be implemented in COMSOL as follows

```

disp_x = (at3(offset,offset,z, u) + at3(-offset,offset,z, u) +
          at3(-offset,-offset,z, u) + at3(offset,-offset,z, u))/4
disp_y = (at3(offset,offset,z, v) + at3(-offset,offset,z, v) +
          at3(-offset,-offset,z, v) + at3(offset,-offset,z, v))/4

```

Here the quantities  $u$  and  $v$  correspond to the displacement in  $x$  or  $y$  direction, respectively. The constant `offset` is set to 10 mm such that the probe lines are located close to the irises but still entirely within the solid.

Fig. 24 shows the radial displacement of the center axis due to thermal expansion along the TD26\_R05\_CC prototype assembly at various flow rates and average RF power. The position  $z = 0$  corresponds to the longitudinal center of the structure which is about 240 mm long. The constraint in accordance to Fig, 22(a) keeps the axial center in the beginning of the structure near its original position. With increasing  $z$ , the axial center displacement rises exponentially up to a few micron if an average RF power of 1 kW or more is applied. The axial center displacement scales approximately linear with the average RF power. It is worth noting that the slopes in Fig. 24 provide slightly different increases towards larger input RF power. For example, at a level of 250 W the overall largest center displacement is obtained at the flow rate of 11/min. By increasing the input RF to 500 W, the resulting displacements at

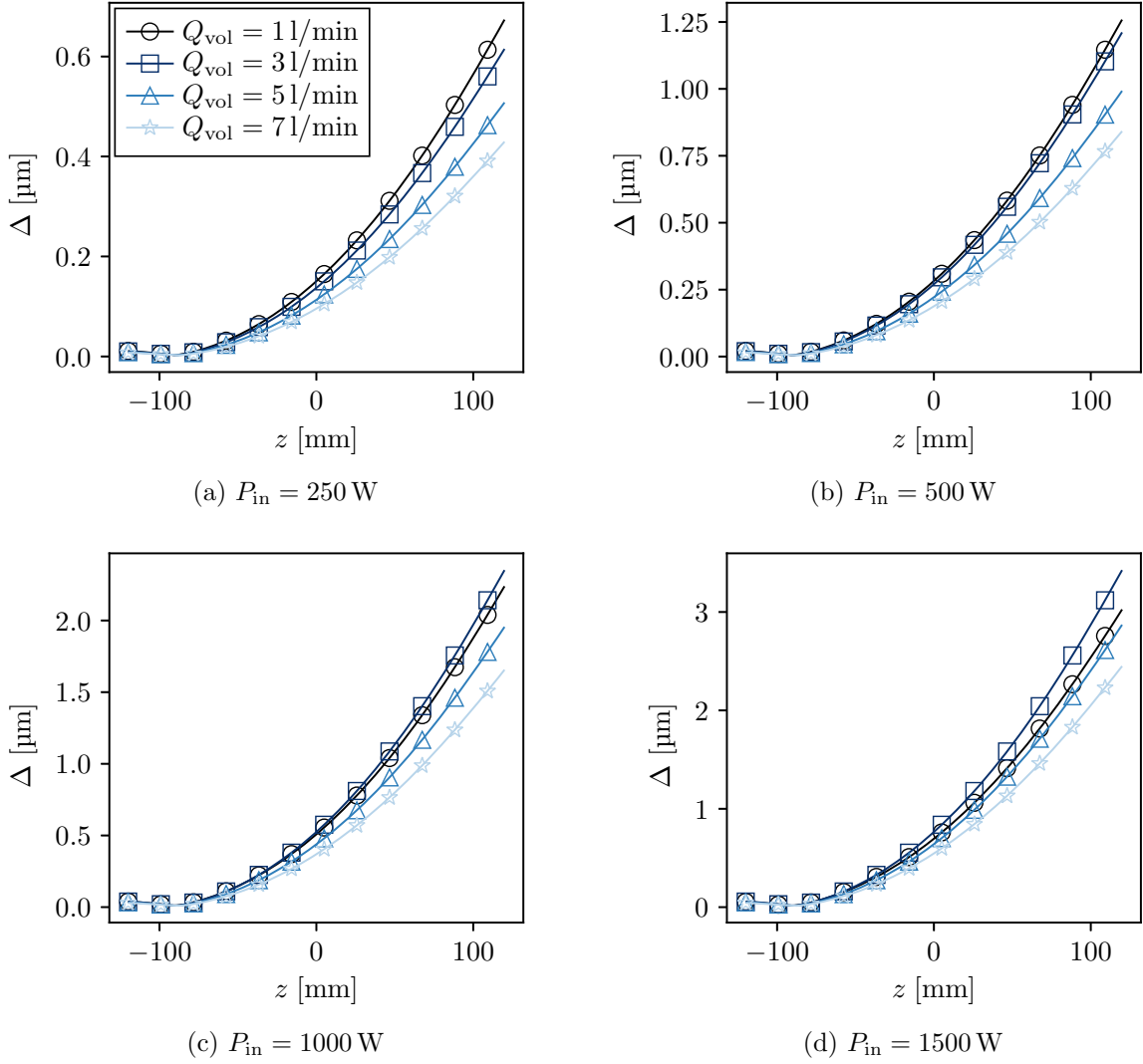


Figure 24: Distance between the beam and the center axis of the deformed TD26\_R05\_CC prototype assembly with single circuit cooling. The input RF power and water flow rate are varied while the air convective heat transfer coefficient, ambient temperature and inlet temperature are fixed to  $5 \text{ W}/(\text{m}^2\text{K})$ ,  $28 \text{ degC}$ , and  $27 \text{ degC}$ , respectively.

11 l/min and 31 l/min water flow are already comparable. By further increasing the power level, a water flow rate of 31 l/min yield larger displacements of the axial center than 11 l/min. The same tendency applies to the even higher flow rates of 51 l/min and 71 l/min which, however, require more than 1500 W average RF power to observe the same effect with regard to 11 l/min water flow.

The axial center displacement in the transverse plane along the TD26\_R05\_CC prototype assembly was further studied for the different cooling circuit from Sec. 3.2. Fig. 24 illustrates the radial displacement field of the solid at the structure exit according to the case studies in Fig. 19. Both circuits with symmetric paths reveal a coaxial distribution of the displacement field. Hence, the center axis remains at its original location. This is confirmed by Fig. 26(a)



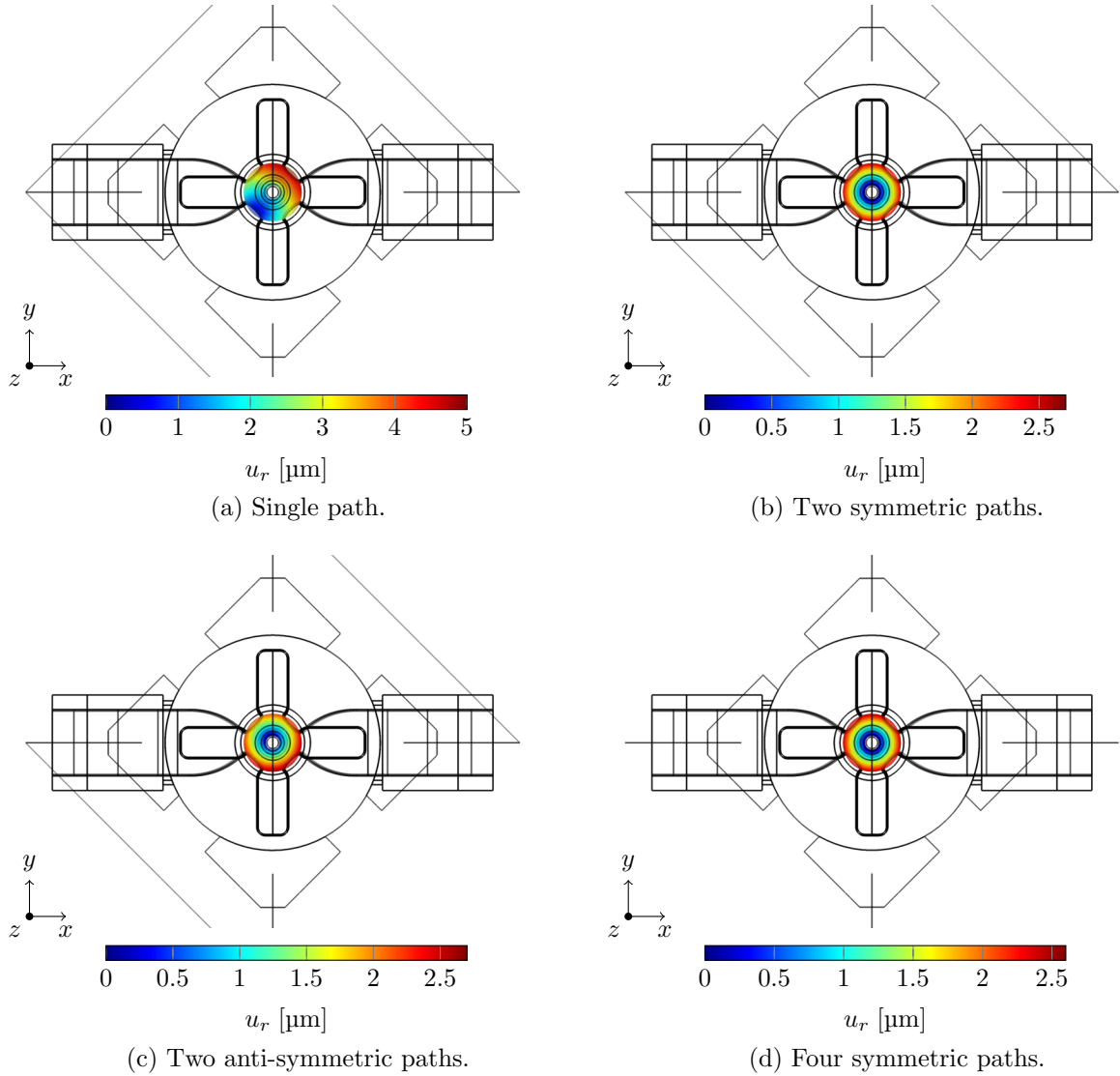


Figure 25: Cross-sectional view of the radial deformation due to thermal expansion of the TD26\_R05\_CC assembly at the exit provided various cooling paths, each with an input RF power, water flow rate, and air convective heat transfer coefficient being 1 kW, 31/min and 5 W/(m<sup>2</sup>K), respectively. An ambient temperature of 28 degC is assumed while the water temperature is set to 27 degC at the corresponding inlets.

and (b) which show the displacement of the axial center in  $x$  and  $y$ -direction, respectively, from its original location along the structure. The fact that both components vanishes for the cooling circuits with either two or four symmetric paths means that only a quarter of the model is sufficient to simulate its combined RF, thermal, and structural behavior. Note, by introducing two symmetry planes to the applied COMSOL model, the computational time reduces by approximately one order of magnitude.

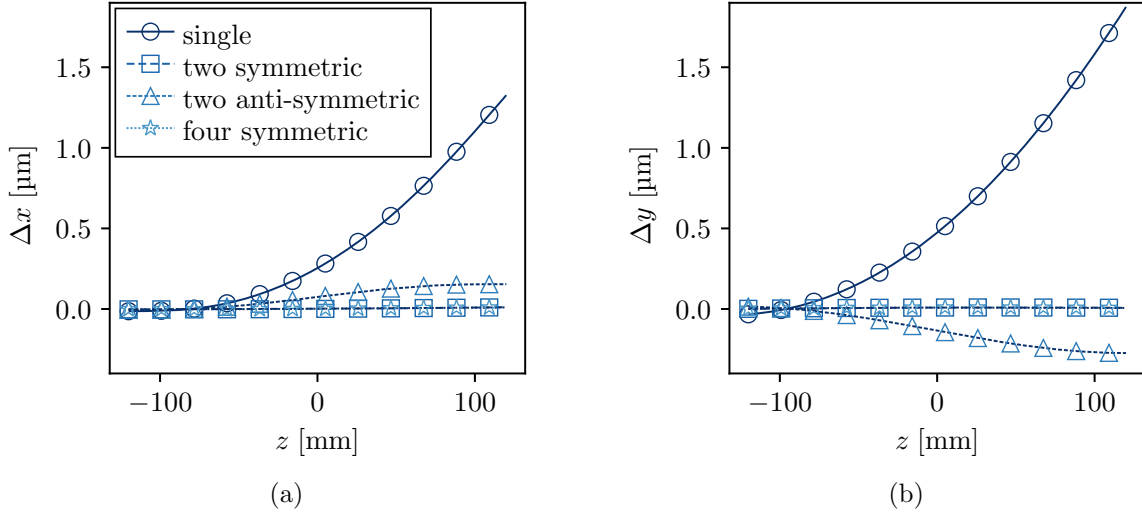


Figure 26: Transverse displacement of the axial center in  $x$  and  $y$  direction from its original position due to thermal expansion of the TD26\_R05\_CC prototype assembly, with the input RF power, water flow rate, and air convective heat transfer coefficient being 1 kW, 31/min and 5 W/(m<sup>2</sup>K), respectively. An ambient temperature of 28 degC is assumed while the water inlet temperature is set to 27 degC. The results are referred to different cooling circuits according to Fig. 19.

### 3.4 Moving Mesh and Port Displacement

In order to study the impact of thermal expansion or contraction on the RF behavior of the traveling wave structures, it is necessary to transfer the displacement field onto the vacuum part. There are various approaches available, for instance, geometry modification, mesh displacement, or the use of perturbation theory. The latter one is typically restricted to small deformations while changes in geometry or directly within the mesh are generally applicable. A detailed study on this subject can be found in [17]. The preferred method in COMSOL considers instant mesh manipulations [18]. A dedicated module called *Moving Mesh* allows to transfer the structure deformation due to thermal expansion or contraction onto the mesh which is associated with the inner volume filled with vacuum. It is important to note that this domain is naturally not involved in the structural simulations. Hence, the displacement field on the interior surface is used as a boundary condition for moving nodes of the vacuum mesh.

A particular difficulty is the treatment of RF and beam pipe ports as they are not bounded by the solid part, hence, they are open. Consequently, there is no solution of the displacement vector field  $\mathbf{u}$  available that could serve as a boundary condition for mesh displacements. However, keeping the ports at their original position yield artificial RF reflections due to mesh distortions. The same is true for symmetry planes if applied. To move the RF and beam pipe ports consistently with the surrounding structure, the displacement vector field

$\mathbf{u}$  can be obtained by solving the following problem within the particular port surface  $\partial\Omega_p$

$$\nabla(\nabla \cdot \mathbf{u}) = 0, \quad \mathbf{r} \in \partial\Omega_p, \quad (40)$$

$$\mathbf{u} = \mathbf{u}_0, \quad \mathbf{r} \in \partial\Omega_p \cap \partial\Omega_{\text{solid}}. \quad (41)$$

Here,  $\mathbf{u}_0$  refers to the solution of problem (38) within the solid part, and is used as Dirichlet boundary condition at the port edges in (41). The set of partial differential equations is solved for each RF or beam pipe port individually before moving the interior mesh associated with vacuum. The same is true for symmetry boundaries if available. Fig. 27 illustrates such a interior mesh displacement in accordance to the structural deformation of the TD26\_R05\_CC prototype assembly with single cooling circuit. The same RF and thermal conditions apply as in Fig. 23. The two highlighted regions show mesh displacements at ports, with the solid gray parts being the original geometry while the colored solid parts corresponds to the thermal expanded structure. Note, all displacements are scaled with a factor of 100 for visualization. It can be seen already that the mesh quality seem to be preserved during displacement by using (40) and (41). Eventually, this was proven by subsequent RF simulations applied on the perturbed vacuum mesh.

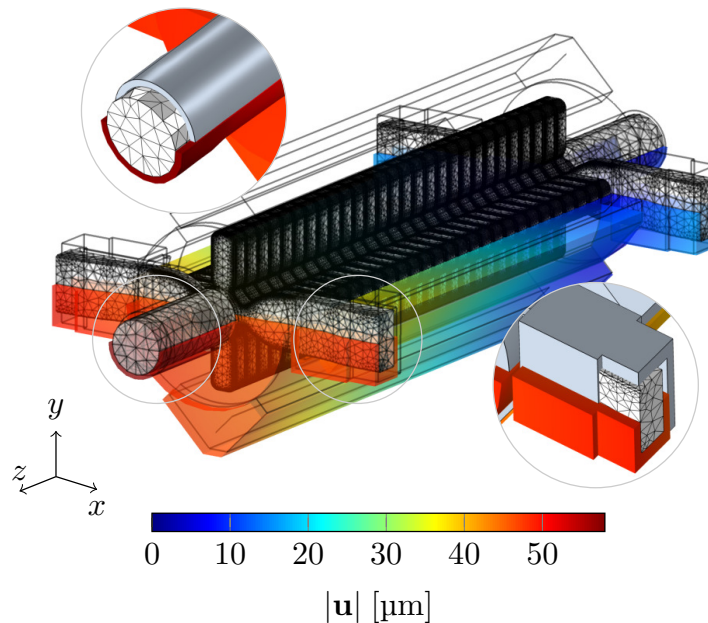


Figure 27: Vacuum mesh displacement according to the structure deformation. The displacement of open regions such as RF or beam pipe ports are obtained from solving a local Laplace-like equation taking into account the surrounding structural deformation as Dirichlet boundary condition. The solid gray part in the highlighted regions corresponds to the original geometry. For visualization, displacements are amplified by a factor of 100.

## 4 Studies on Perturbed Structures

The impact of thermal expansion or contraction of the RF behavior of traveling wave structures is best seen from the cell-to-cell phase advance and internal reflection according to

Sec. 3.1. In contrast, the scattering matrix, which is directly measurable, provides RF reflections and transmissions only at the input and output ports. Figs. 28(a) and (b) illustrate how the cell-to-cell phase advance and internal reflection, respectively, change for both prototype assemblies if thermal and structure-mechanical aspects are taken into account. For this initial example, an input RF power of 1 kW and water flow rate of 3 l/min were chosen. Based on the results of [13], the ambient and water inlet temperatures were set to 28 degC and 27 degC, respectively, while the air convective heat transfer coefficient is 5 W/(m<sup>2</sup>K).

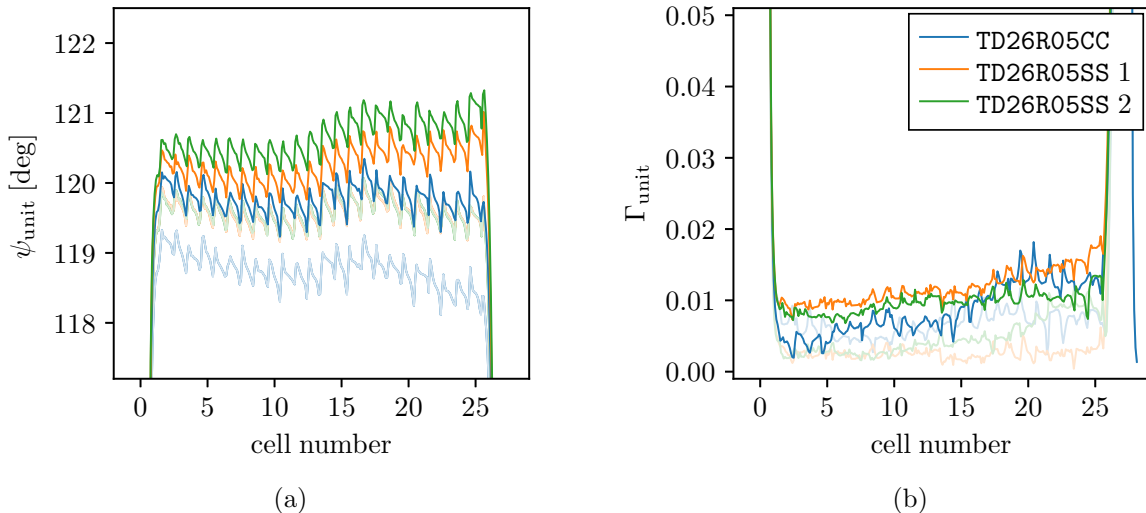


Figure 28: (a) Cell-to-cell phase advance and (b) internal reflection for different prototype assemblies taking into account thermal deformations. The input RF power, water flow rate, and air convective heat transfer coefficient are 1 kW, 3 l/min and 5 W/(m<sup>2</sup>K), respectively. An ambient temperature of 28 degC is assumed while the water inlet temperature of the individual single cooling circuit according to Fig. 3 is set to 27 degC. For comparison, the phase advance and reflection of the original structures are shown in light colors.

Note, the TD26\_R05\_CC prototype assembly is by design not tuned which explains the phase advance around 119 deg on average in light blue in Fig. 28(a). By accounting for the above mentioned thermal and structure-mechanical conditions the deviation from the desired phase advance of 120 deg coincidentally vanishes as shown by the blue curve in the same figure. Generally, the cell-to-cell phase advance at fixed frequency increases on average along the structure when taking thermal expansion into account. This is not necessarily true for internal reflections as shown by subsequent studies which involve the variation of water flow rate, different cooling circuits, comparison to linear scaled geometries, as well as the frequency tuning by changing the water inlet temperature.

#### 4.1 Variation of Flow Rate

Figs. 29 and 30 show the cell-to-cell phase advance and reflection, respectively, at various water flow rates and input RF powers applied on the TD26\_R05\_CC prototype assembly. In all cases, the phase advance along the structure is equal or larger than the phase advance

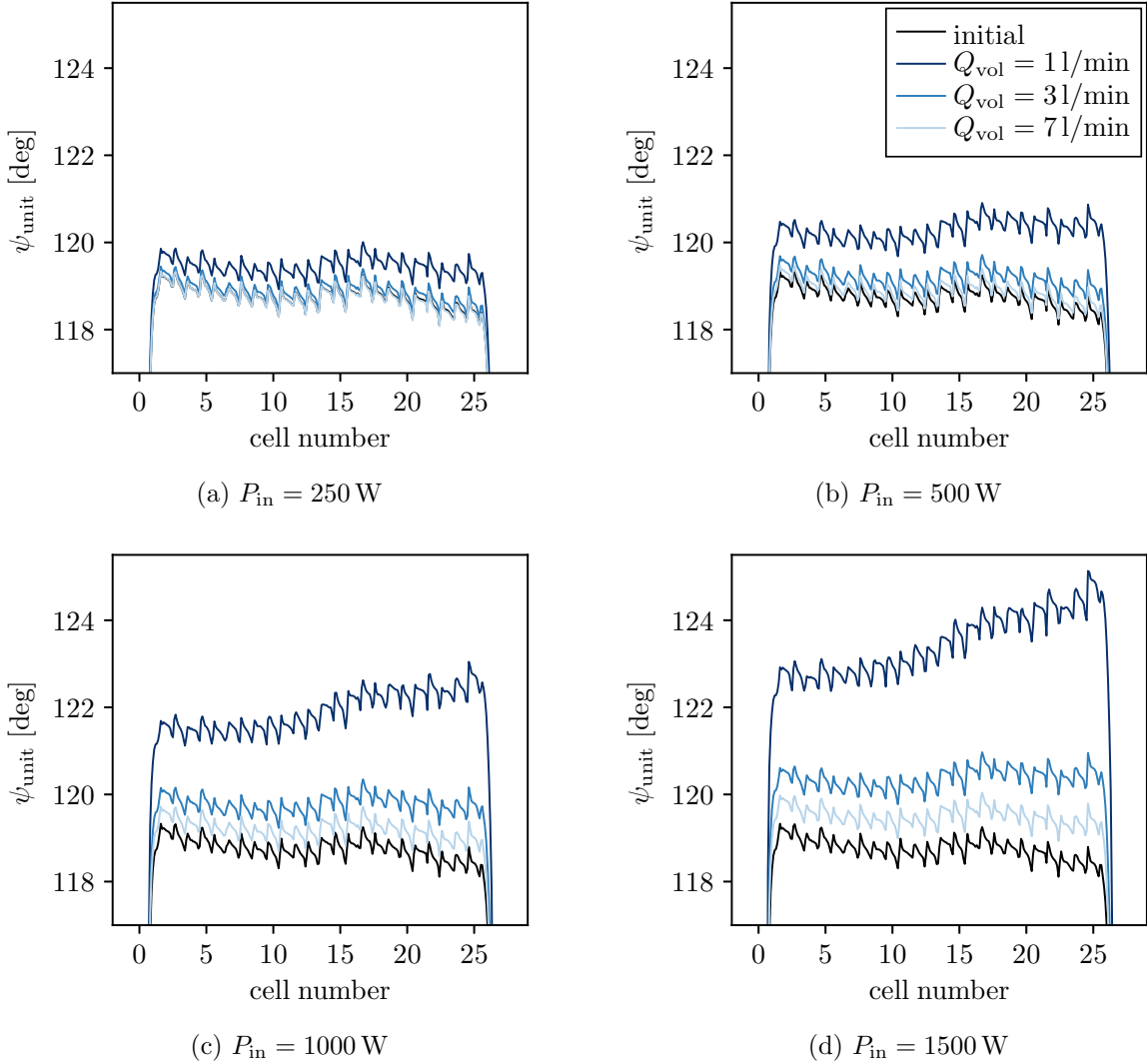


Figure 29: Cell-to-cell phase advance of the TD26\_R05\_CC prototype assemblies taking into account thermal deformations. The input RF power and water flow rate are varied while ambient and water inlet temperature are set to 28 degC and 27 degC, respectively. The single cooling circuit of Fig. 3 (b) is considered. The air convective heat transfer coefficient is 5 W/(m<sup>2</sup>K). In black, the phase advance of the original unperturbed structures.

provided by the original structure, which is highlighted in black in Fig. 29. At almost laminar flow conditions, hence, at a flow rate of 11/min, both, the cell-to-cell phase advance and reflection notably deviate from the original profiles. Already at 250 W input RF power the phase advance is increased by approximately 0.5 deg on average according to Fig. 29(a). In contrast, the impact of thermal expansion on internal reflections at this power level is negligible as shown in Fig. 30(a). Above 500 W input RF power, the threshold of 2% reflection factor is exceeded. By increasing the water flow rate to 31/min the same threshold is almost kept until a power level of 1500 W as depicted in Fig. 30(d). Likewise, the deviation of the cell-to-cell phase advance from the original profile drastically reduces when increasing

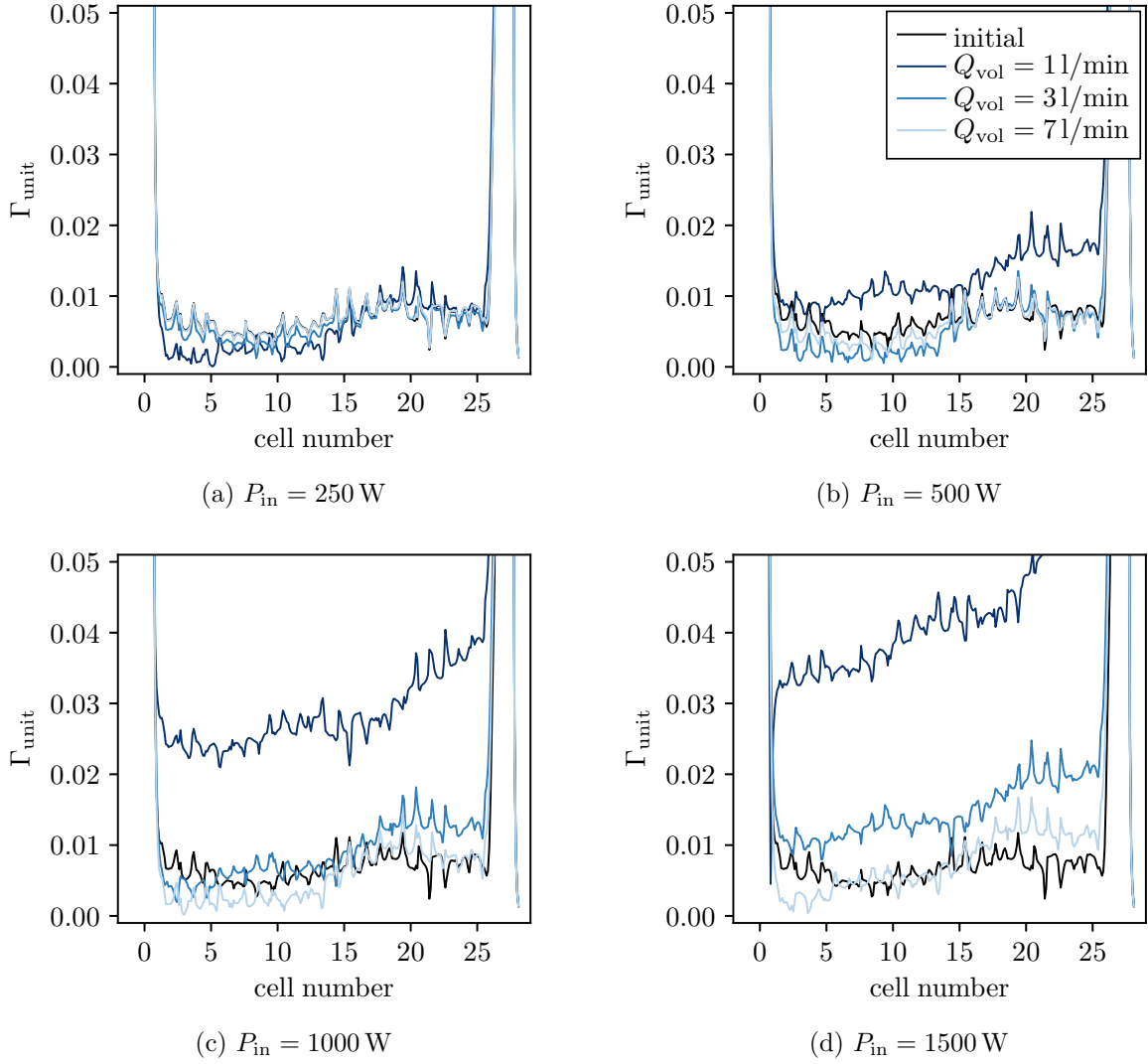


Figure 30: Internal reflection of the TD26\_R05\_CC prototype assemblies taking into account thermal deformations. The input RF power and water flow rate are varied while ambient and water inlet temperature are set to 28 degC and 27 degC, respectively. The single cooling circuit of Fig. 3 (b) is considered. The air convective heat transfer coefficient is  $5 \text{ W}/(\text{m}^2\text{K})$ . In black, the internal reflection of the original unperturbed structures.

the flow rate from 11/min to 31/min as pointed out in Fig. 29(d). The remaining deviation of about 1.5 deg can be slightly lowered by further increasing the flow rate.

## 4.2 Cooling Circuits

Fig. 31 shows the cell-to-cell phase advance and reflection at fixed input RF power and flow rate of 1000 W and 31/min but for various cooling circuits applied on the TD26\_R05\_CC prototype assembly according to Fig. 19. Given the results of [13], the ambient and water inlet temperatures were chosen to be 28 degC and 27 degC, respectively, while the air convective

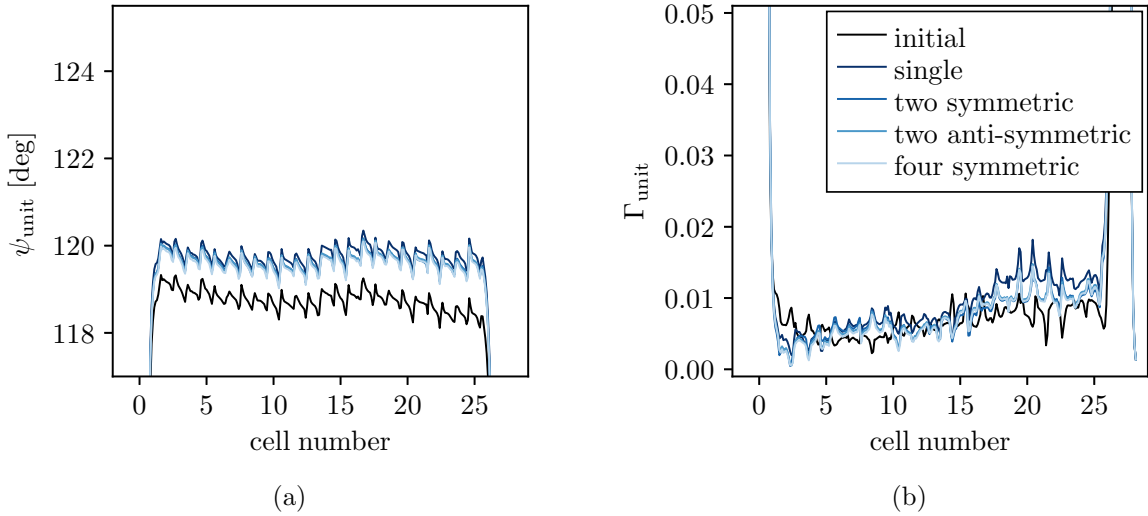


Figure 31: (a) Cell-to-cell phase advance and (b) internal reflection of the TD26\_R05\_CC prototype assemblies taking into account thermal deformations. Different cooling paths according to Fig. 19 are compared to each other. The input RF power, water flow rate, and air convective heat transfer coefficient are 1 kW, 3 l/min, and 5 W/(m<sup>2</sup>K), respectively. An ambient temperature of 28 degC is assumed while the water temperature at the inlets is 27 degC. In black, the phase advance or internal reflection of the original unperturbed structures.

heat transfer coefficient is 5 W/(m<sup>2</sup>K).

Despite of the transversely displaced center axis along the structure in presence of the single cooling circuit and circuit with two anti-symmetric paths, the RF behavior by means of cell-to-cell phase advance and reflection is nearly the same for all considered cooling paths. Consequently, both RF quantities are dominated by parameters such as flow rate, water inlet temperature, and input RF power. However, the detailed connection between predefined cooling pipes plays a minor role here. Furthermore, it was found that the transverse RF field along the structure remains within numerical noise even though the beam line is transversely displaced from the structure center by more than 2 μm at the output in according to the single cooling circuit in Fig. 26.

### 4.3 Linear Scaling

The minor impact on RF behavior given by the beam displacement from center axis as previously observed suggests a comparison between real deformed and linear scaled structures. Since the latter ones equal the original but scaled model, there is no need to involve anymore the moving mesh step of Sec. 3.4 in the analyses. Moreover due to the linear and isotropic scaling, only a quarter of the perturbed structure need to be considered as illustrated in Fig. 7(b). As example, let the TD26\_R05\_CC prototype assembly as depicted in Fig. 3(a) be considered, with an input RF power of 1500 W being applied. The ambient and water inlet temperature are 28 degC and 27 degC, respectively, while the air convective heat transfer is assumed 5 W/(m<sup>2</sup>K).



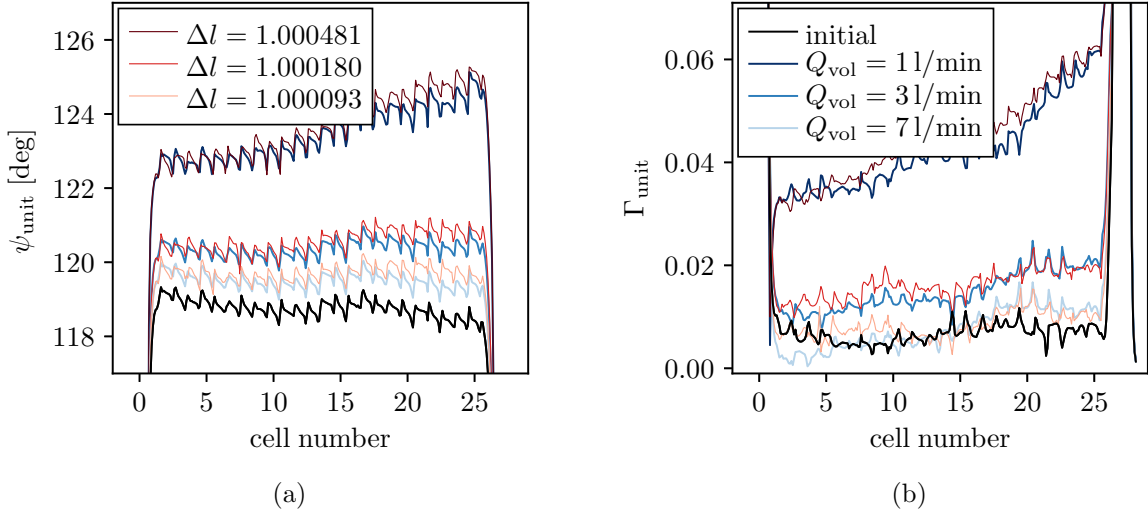


Figure 32: Thermal study of the TD26\_R05\_CC prototype assembly with different cooling paths according to Fig. 19. The input RF power and air convective heat transfer coefficient are 1.5 kW, and 5 W/(m<sup>2</sup>K), respectively. An ambient temperature of 28 degC is assumed while the water temperature at the inlets is 27 degC. (a) Cell-to-cell phase advance and (b) Internal reflection, both based on the periodic voltage standing wave ratio method.

Fig. 32(a) and (b) show the cell-to-cell phase advance and reflection, respectively, at three different water flow rates in the single cooling circuit. The RF quantities of real deformed structures highlighted in blue are well described by the linearly scaled models whose phase advance and internal reflections are shown in red. The scaling factors correspond to the relative length variation in longitudinal direction. Note, for this particular example, the transverse expansions were found to be between 5% to 20% larger than the longitudinal ones depending on the flow rate. Consequently, the impact of thermal expansion on the RF behavior of CLIC traveling wave structure is well described by linearly scaled models according to the thermal expansion in longitudinal direction. The fact that asymmetric deformation due to cooling schemes have minor influence on cell-to-cell phase advance and reflections, significantly reduce the simulation effort.

#### 4.4 Frequency Tuning by Water Temperature

The structures are designed at a specific frequency and temperature. Changing one parameter generally requires to adjust the other one as well in order maintain cell-to-cell advance and RF reflection. This is studied in Fig. 33 for the TD26\_R05\_CC prototype assembly at fixed input RF power, water flow rate, and air convective heat transfer coefficient are 1 kW, 31/min, and 5 W/(m<sup>2</sup>K), respectively. Other than before, the inlet temperature is reduced to 10 degC while the ambient temperature remains at 28 degC. It was found that, both profiles, the cell-to-cell phase advance and internal reflection were nearly preserved at a frequency of 11.996 GHz under such thermal conditions while structure is designed at a frequency and temperature of 11.994 GHz and 28 degC.



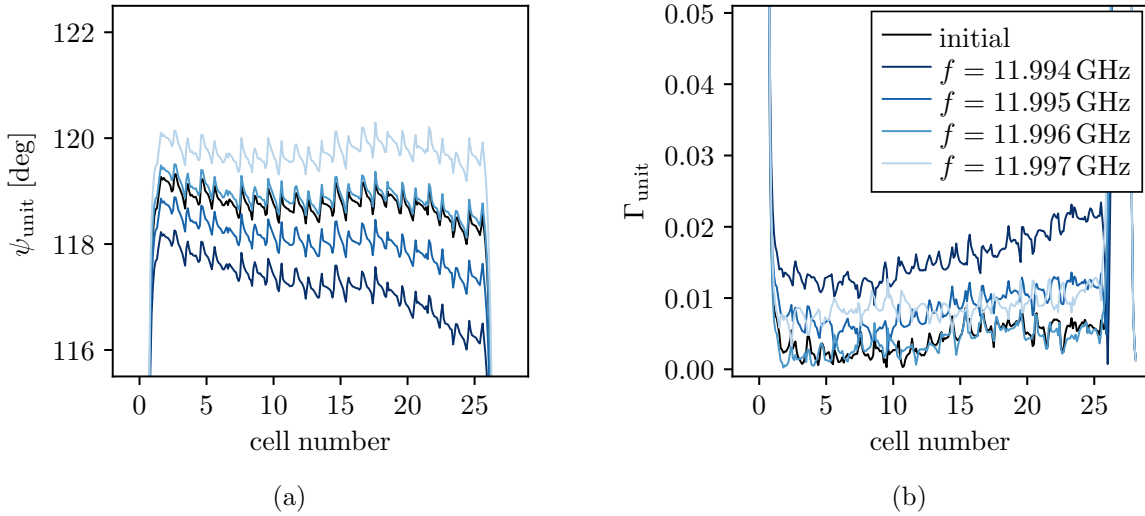


Figure 33: (a) Cell-to-cell phase advance and (b) internal reflection of the TD26\_R05\_CC prototype assemblies at different frequencies taking into account thermal deformations. The input RF power, water flow rate, and air convective heat transfer coefficient are 1 kW, 31/min, and 5 W/(m<sup>2</sup>K), respectively. Other than before, the inlet temperature is reduced to 10 degC while the ambient temperature remains at 28 degC. In black, the phase advance or internal reflection of the original unperturbed structures at the design frequency of 11.994 GHz.

## 5 Conclusions

The performed study aimed at establishing the acceptable range of variation of relevant thermo-mechanical quantities able to provide still satisfactory operation of CLIC accelerating structures by means of numerical models and simulations. The study was able to show that a fully consistent model can be built, which allows to observe the structural deformation of the RF device under nominal operating conditions and to feed back the deformed mesh to study the consequences on RF figures of merit. Realistic operational parameters have been used in the simulations, in terms of dissipated power, water flow and temperature.

The results show that the transverse deformation of the accelerating structure is kept within few microns with nominal power dissipation and water flow; also, with the given water circuit, saturation is reached after the value of 5 l/min water flow and a further increase of flow does not produce any significant improvements.

The cell-to-cell phase advance and the local reflection coefficient have demonstrated to be sufficiently sensitive to temperature variations and hence to structure deformations. They result to be significant quantities to evaluate how stable the chosen operating conditions are. In particular the cell-to-cell phase advance is very sensitive to water flow and temperature changes at nominal power dissipation. It can be used to establish the appropriate specification for the water control and to allow a fine “tuning” of the cooling regime for optimum performance.

In the end it has been demonstrated that the results obtained by the deformed mesh approach, in the studied small deformation regime, can be well reproduced by linear scaled structures, by considering linear and isotropic scaling, so considerably simplifying and speed-

ing up studies in the future.

## 5.1 Simulation approach

A general approach was presented to evaluate traveling wave RF parameter by convolution integrals (12), (13), and (18). Typically, the parameters are evaluated for individual cells and interpolated in between whereas the convolution integral is calculated at arbitrary position along the structure (Fig. 6b). It was found that a smooth rectangular window over a cell length improves the result quality (Fig. 10b).

## 5.2 Pipe flow

A flow rate of at least 3l/min should be considered not to increase the phase advance by more than 2 deg over an average power range up to 1500 W (Fig. 29). More than 4l/min flow rate is not reasonable due to saturating behavior of the heat transfer (Fig. 18). Much rougher pipe surface at 3l/min provides a similar heat transfer coefficient on average as a smooth pipe at 4l/min. It remains open which option is favorable in with regard to cavitation.

## 5.3 RF results

Transverse displacements of the beam from the center axis are too small to have notable impact on phase advance and internal reflection (Fig. 31). There is no need to apply the real deformation in order to study the RF behavior of perturbed structures. Scaling according to the longitudinal thermal expansion or contraction is sufficient (Fig. 32). Furthermore, Phase advance and internal reflection are fully preserved when changing the temperature in order to adjust frequency. For the present structures at 11.994 GHz nominal, the frequency can be realistically varied by  $\pm 2$  MHz (Fig. 33).

## Acknowledgment

The authors would like to thank Alex Vamvakas and Henri Berg for their preliminary studies towards the present work. We acknowledge the fruitful and regular discussions with Markus Aicheler, Matthew Capstick and Steffen Doebert, and like to thank Alexej Grudiev, Amos Dexter, and Walter Wuensch for their valuable suggestions.

## References

- [1] A. Grudiev, “RF design and parameters of 12 GHz TD26\_vg1.8\_R05\_CC,” CERN, Geneva, Switzerland, Tech. Rep. 1078698 v.1, Mar 2017. [Online]. Available: <https://edms.cern.ch/document/1078698/1>
- [2] *ANSYS - ANalysis SYStem Ver. R19.1*, ANSYS Inc., Canonsburg, Pennsylvania, USA, 2019. [Online]. Available: [www.ansys.com](http://www.ansys.com)
- [3] COMSOL Knowledge Base, “The usage of form union and form assembly.” [Online]. Available: <https://www.comsol.com/support/knowledgebase/1216/>
- [4] W. Frei, “Improving your meshing with partitioning.” [Online]. Available: <https://www.comsol.de/blogs/improving-your-meshing-with-partitioning/>
- [5] J. Van Bladel, *Electromagnetic Fields*, 2nd ed. John Wiley & Sons, 2007.
- [6] B. Schieche, “Overview of integration methods in space and time.” [Online]. Available: <https://www.comsol.com/blogs/overview-integration-methods-space-time/>
- [7] N. M. Kroll, C.-K. Ng, and D. C. Vier, “Applications of time domain simulation to coupler design for periodic structures,” in *Proc. XX International Linac Conference (LINAC’00), Monterey, California (USA), 21-25 August 2000*. Monterey, California (USA): JACoW Publishing, Aug 2000, paper TUE04, pp. 614–617.
- [8] C. Ruhl, “Analyze your simulation results with projection operators.” [Online]. Available: <https://www.comsol.com/blogs/analyze-simulation-results-projection-operators/>
- [9] A. Lunin, V. Yakovlev, and A. Grudiev, “Analytical solutions for transient and steady state beam loading in arbitrary traveling wave accelerating structures,” *Phys. Rev. ST Accel. Beams*, vol. 14, p. 052001, 2011.
- [10] Y. A. Cengel, *Heat Transfer: A Practical Approach*, 2nd ed. New York, NY: McGraw-Hill Professional, 2002.
- [11] B. Petukhov, “Heat transfer and friction in turbulent pipe flow with variable physical properties,” ser. *Advances in Heat Transfer*, J. P. Hartnett and T. F. Irvine, Eds. Elsevier, 1970, vol. 6, pp. 503 – 564. [Online]. Available: <http://www.sciencedirect.com/science/article/pii/S0065271708701539>
- [12] C. S.W., “Friction factor equations spans all fluid-flow regimes.” *Chem. Eng.*, vol. 84, no. 24, pp. 91 – 92, Nov 1977.
- [13] C. W. E. Lam, A. Vamvakas, M. Aicheler, J. I. Vainola, and S. Doebert, “Thermal control for the two-beam module of the compact linear collider with computational fluid dynamics simulations of conjugate heat transfer problems, with subsidiary finite-element simulations,” CERN, Geneva, Tech. Rep. CERN-ACC-2018-0031. CLIC-Note-1081, Jun 2018. [Online]. Available: <https://cds.cern.ch/record/2642576>

- [14] COMSOL, “Cooling of an injection mold.” [Online]. Available: <https://www.comsol.de/model/cooling-of-an-injection-mold-12371>
- [15] A. C. Eringen and E. S. Şuhubi, *Elastodynamics: Linear theory*, ser. Elastodynamics. Academic Press, 1974, vol. II, no. Vol. II. [Online]. Available: <https://books.google.de/books?id=0wtQNAEACAAJ>
- [16] V. Paramonov, B. Militsyn, and A. Skassyrskaya, “Parameters stability of s-band rf gun cavity due to effects of pulsed rf heating,” *Nuclear Instruments and Methods in Physics Research Section A: Accelerators, Spectrometers, Detectors and Associated Equipment*, vol. 940, pp. 337 – 343, Oct 2019. [Online]. Available: <http://www.sciencedirect.com/science/article/pii/S0168900219308927>
- [17] K. Papke, A. Carvalho, C. Zanoni, and A. Grudiev, “Design studies of a compact superconducting rf crab cavity for future colliders using Nb/Cu technology,” *Physical Review Accelerators and Beams*, vol. 22, 07 2019.
- [18] E. Dickinson, “Model deforming objects with the arbitrary lagrangian-eulerian method.” [Online]. Available: <https://www.comsol.de/blogs/model-deforming-objects-with-the-arbitrary-lagrangian-eulerian-method/>

## A Parameters

Table 1: Parameters of the TD26\_R05\_CC prototype assembly.

Parameter	Value	Description
Cell_Period	8.332 mm	Cell period.
Pipe_X1	0.0 mm	1 <sup>st</sup> x-coordinate of cooling path.
Pipe_X2	45.0 mm	2 <sup>nd</sup> x-coordinate of cooling path.
Pipe_Y1	45.0 mm	1 <sup>st</sup> y-coordinate of cooling path.
Pipe_Y2	0.0 mm	2 <sup>nd</sup> y-coordinate of cooling path.
Pipe_Z1	-114.393 mm	1 <sup>st</sup> z-coordinate of cooling path.
Pipe_Z2	-86.0 mm	2 <sup>nd</sup> z-coordinate of cooling path.
Pipe_Z3	86.0 mm	3 <sup>rd</sup> z-coordinate of cooling path.
Pipe_Z4	111.307 mm	4 <sup>th</sup> z-coordinate of cooling path.
Pipe_Diameter	8 mm	Diameter of cooling channel.
Pipe_SurfRoughness	0.0025 mm	Surface roughness of cooling channel.
Pipe_Qvol	6 l/min	Coolant volume flow rate.
T_ambient	28 degC	Ambient temperature.
T_inlet	27 degC	Inlet temperature of the coolant.
HTC_CuAir	5 W/(m <sup>2</sup> K)	Heat transfer coefficient Cu to air.
RF_PhaseOffset	0 deg	Phase correction between both input signals.
RF_PortName	1	Port name.
RF_Power	2100 W	Total RF power entering the input ports.

Table 2: Parameters of the TD26\_R05\_SS prototype assembly (super structure).

Parameter	Value	Description
Cell_Period	8.332 mm	Cell period.
Pipe_X11	17.5 mm	1 <sup>st</sup> x-coordinate of cooling path, structure 1.
Pipe_X21	44.0 mm	2 <sup>nd</sup> x-coordinate of cooling path, structure 1.
Pipe_X12	17.5 mm	1 <sup>st</sup> x-coordinate of cooling path, structure 2.
Pipe_X22	44.0 mm	2 <sup>nd</sup> x-coordinate of cooling path, structure 2.
Pipe_Y11	44.0 mm	1 <sup>st</sup> y-coordinate of cooling path, structure 1.
Pipe_Y21	17.5 mm	2 <sup>nd</sup> y-coordinate of cooling path, structure 1.
Pipe_Y12	45.0 mm	1 <sup>st</sup> y-coordinate of cooling path, structure 2.
Pipe_Y22	17.5 mm	2 <sup>nd</sup> y-coordinate of cooling path, structure 2.
Pipe_Z11	-228.4941 mm	1 <sup>st</sup> z-coordinate of cooling path, structure 1.
Pipe_Z21	-215.9641 mm	2 <sup>nd</sup> z-coordinate of cooling path, structure 1.
Pipe_Z31	-27.0671 mm	3 <sup>rd</sup> z-coordinate of cooling path, structure 1.
Pipe_Z41	-15.2071 mm	4 <sup>th</sup> z-coordinate of cooling path, structure 1.
Pipe_Z12	36.0560 mm	1 <sup>st</sup> z-coordinate of cooling path, structure 2.
Pipe_Z22	36.0560 mm	2 <sup>nd</sup> z-coordinate of cooling path, structure 2.
Pipe_Z32	216.634 mm	3 <sup>rd</sup> z-coordinate of cooling path, structure 2.
Pipe_Z42	227.294 mm	4 <sup>th</sup> z-coordinate of cooling path, structure 2.
Pipe_Diameter	8 mm	Diameter of cooling channel.
Pipe_SurfRoughness	0.0025 mm	Surface roughness of cooling channel.
Pipe_Qvol	6 l/min	Coolant volume flow rate.
T_ambient	28 degC	Ambient temperature.
T_inlet	27 degC	Inlet temperature of the coolant.
HTC_CuAir	5 W/m <sup>2</sup> /K	Heat transfer coefficient Cu to air.
RF_PhaseOffset	0 deg	Phase correction between both input signals.
RF_PortName	1	Port name.
RF_Power	2100 W	Total RF power entering the input ports.

## B Selections

Table 3: Selections of the TD26\_R05\_CC prototype assembly.

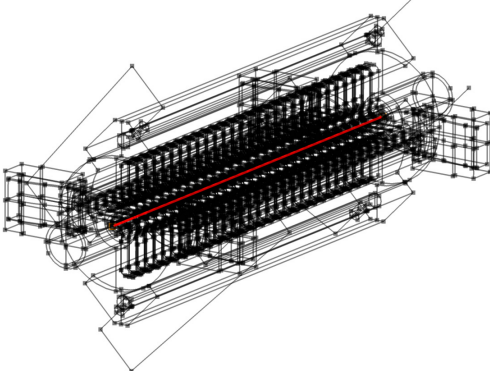
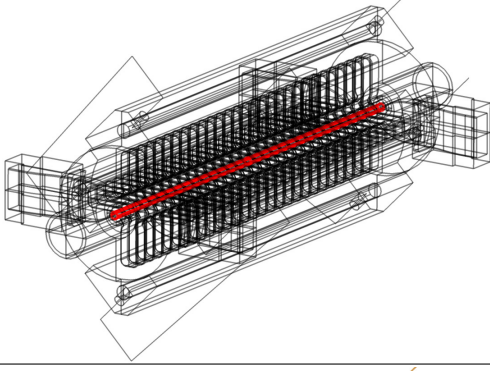
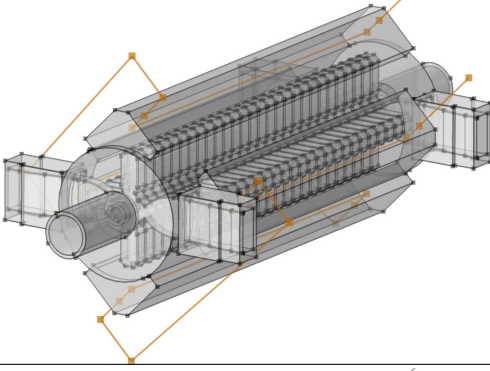
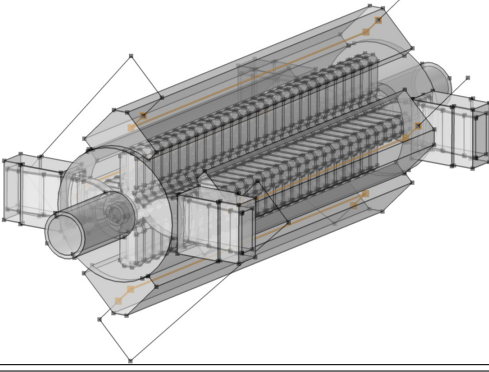
Name	Description	View
Beam Line	Edge along the nominal particle beam.	
Beam Cylinder	Boundaries of the cylinder enveloping the beam line.	
Cooling Pipe	Edges associated with the cooling circuit.	
Inner Cooling Pipe	Edges associated with the cooling circuit which are inside the structure.	



Table 4: Selections of the TD26\_R05\_CC prototype assembly.

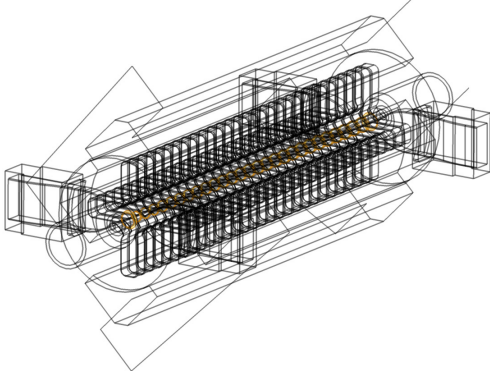
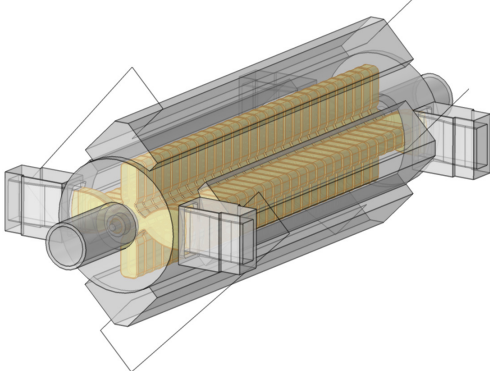
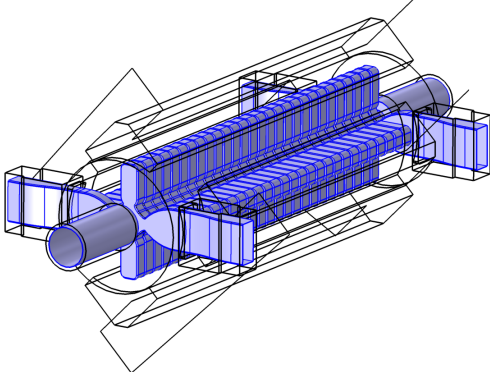
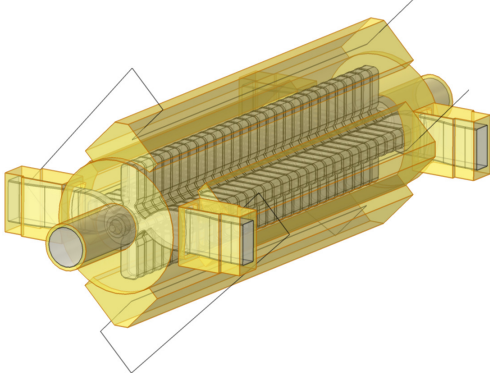
Name	Description	View
Iris	Boundaries associated with the irises using a cylindrical selection.	
Waveguide	Boundaries associated with waveguides and couplers using a cylindrical selection. The iris boundaries are excluded.	
Inner Surface	Boundaries between the vacuum part and the structure.	
Outer Surface	Remaining boundaries of the structure which are not associated with Inner Surface.	

Table 5: Selections of the TD26\_R05\_CC prototype assembly.

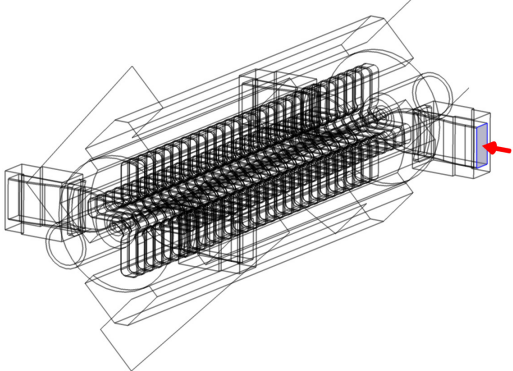
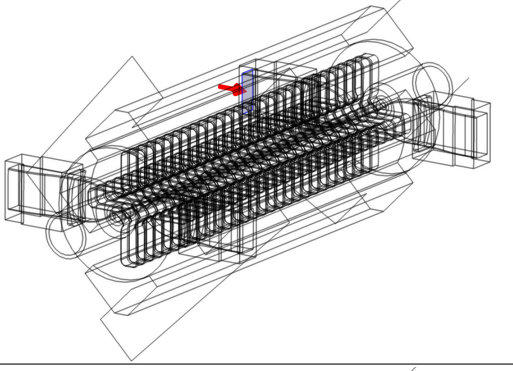
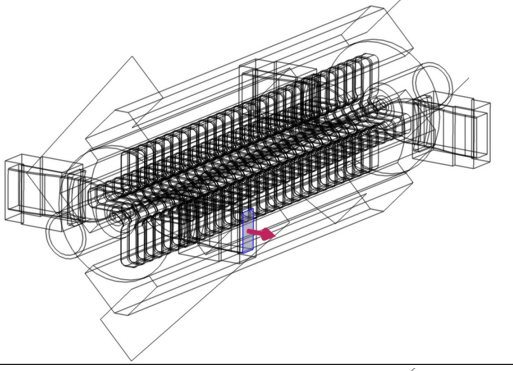
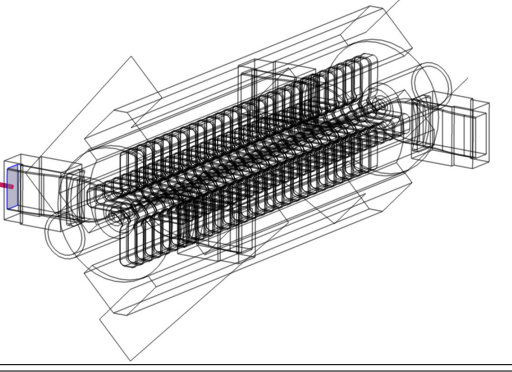
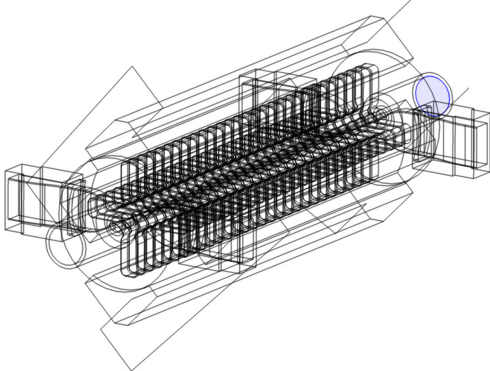
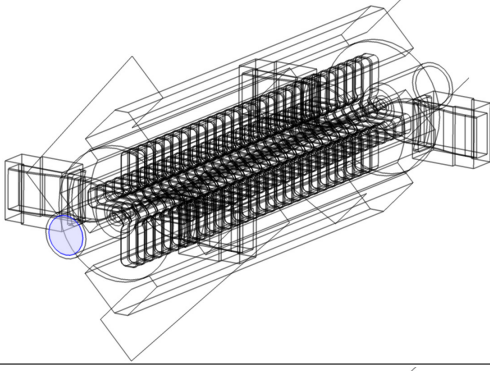
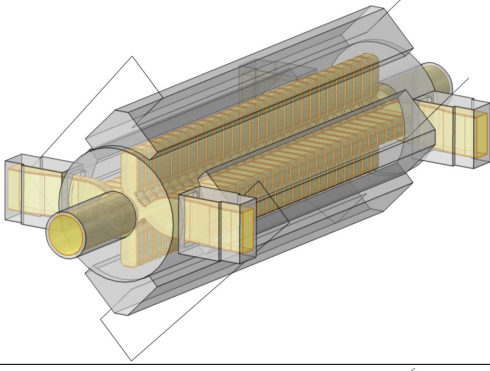
Name	Description	View
Port 1	Boundary of the first input port.	
Port 2	Boundary of the second input port.	
Port 3	Boundary of the first output port.	
Port 4	Boundary of the second output port.	

Table 6: Selections of the TD26\_R05\_CC prototype assembly.

Name	Description	View
Beam Port 1	Boundary of the first beam pipe port.	
Beam Port 2	Boundary of the second beam pipe port.	
Vacuum	Domains or boundaries associated with the inner volume filled with vacuum.	
Cavity	Domains or boundaries associated with the structure.	